

<b>REPORT DOCUMENTATION PAGE</b>			2		Form Approved OMB NO. 0704-0188	
<p>The public reporting burden for this collection of information is estimated to average 1 hour per response, including the time for reviewing instructions, searching existing data sources, gathering and maintaining the data needed, and completing and reviewing the collection of information. Send comments regarding this burden estimate or any other aspect of this collection of information, including suggestions for reducing this burden, to Washington Headquarters Services, Directorate for Information Operations and Reports, 1215 Jefferson Davis Highway, Suite 1204, Arlington VA, 22202-4302. Respondents should be aware that notwithstanding any other provision of law, no person shall be subject to any penalty for failing to comply with a collection of information if it does not display a currently valid OMB control number.</p> <p>PLEASE DO NOT RETURN YOUR FORM TO THE ABOVE ADDRESS.</p>						
1. REPORT DATE (DD-MM-YYYY)		2. REPORT TYPE New Reprint		3. DATES COVERED (From - To) -		
4. TITLE AND SUBTITLE A Combined Finite-Element/Discrete-Particle Analysis of a Side-Vent-Channel-Based Concept for Improved Blast-Survivability of Light Tactical Vehicles				5a. CONTRACT NUMBER W911NF-11-1-0518		
				5b. GRANT NUMBER		
				5c. PROGRAM ELEMENT NUMBER 611102		
6. AUTHORS M. Grujicic, R. Yavari, J. S. Snipes, S.Ramaswami, R. Gupta				5d. PROJECT NUMBER		
				5e. TASK NUMBER		
				5f. WORK UNIT NUMBER		
7. PERFORMING ORGANIZATION NAMES AND ADDRESSES Clemson University 300 Brackett Hall Box 345702 Clemson, SC 29634 -5702				8. PERFORMING ORGANIZATION REPORT NUMBER		
9. SPONSORING/MONITORING AGENCY NAME(S) AND ADDRESS (ES) U.S. Army Research Office P.O. Box 12211 Research Triangle Park, NC 27709-2211				10. SPONSOR/MONITOR'S ACRONYM(S) ARO		
				11. SPONSOR/MONITOR'S REPORT NUMBER(S) 60050-EG.23		
12. DISTRIBUTION AVAILABILITY STATEMENT Approved for public release; distribution is unlimited.						
13. SUPPLEMENTARY NOTES The views, opinions and/or findings contained in this report are those of the author(s) and should not be construed as an official Department of the Army position, policy or decision, unless so designated by other documentation.						
14. ABSTRACT The recently proposed concept solution for improving blast-survivability of the light tactical military vehicles is critically assessed using combined finite-element/discrete-particle computational methods and tools. The proposed concept involves the use of side-vent-channels attached to the V-shaped vehicle underbody. Since the solution does not connect the bottom and the roof or pass through the cabin of a light tactical vehicle, this solution is not expected to: (a) reduce the available cabin space; (b) interfere with the vehicle occupants' ability to scout the surroundings; and (c) compromise the vehicle's off-road structural durability/reliability. Furthermore, the concept solution						
15. SUBJECT TERMS Detonation of Shallow Buried Mines, Blast and Soil Ejecta Loading, Discrete-Particle Approach						
16. SECURITY CLASSIFICATION OF:			17. LIMITATION OF ABSTRACT UU	15. NUMBER OF PAGES	19a. NAME OF RESPONSIBLE PERSON Mica Grujicic	
a. REPORT UU	b. ABSTRACT UU	c. THIS PAGE UU			19b. TELEPHONE NUMBER 864-656-5639	

## **Report Title**

A Combined Finite-Element/Discrete-Particle Analysis of a Side-Vent-Channel-Based Concept for Improved Blast-Survivability of Light Tactical Vehicles

### **ABSTRACT**

The recently proposed concept solution for improving blast-survivability of the light tactical military vehicles is critically assessed using combined finite-element/discrete-particle computational methods and tools. The proposed concept involves the use of side-vent-channels attached to the V-shaped vehicle underbody. Since the solution does not connect the bottom and the roof or pass through the cabin of a light tactical vehicle, this solution is not expected to: (a) reduce the available cabin space; (b) interfere with the vehicle occupants' ability to scout the surroundings; and (c) compromise the vehicle's off-road structural durability/reliability. Furthermore, the concept solution attempts to exploit ideas and principles of operation of the so-called "pulse detonation" rocket engines in order to create a downward thrust on the targeted vehicle. To maximize the downward thrust effects and minimize the extent of vehicle upward movement, standard engineering-optimization methods and tools are employed for the design of side-vent-channels. The results obtained confirmed the beneficial effects of the side-vent-channels in reducing the blast momentum, although the extent of these effects is relatively small (3–4%).

---

## REPORT DOCUMENTATION PAGE (SF298) (Continuation Sheet)

---

Continuation for Block 13

ARO Report Number 60050.23-EG  
A Combined Finite-Element/Discrete-Particle Ar...

Block 13: Supplementary Note

© 2013 . Published in ARL Technical Report ARL-TR-6736, Vol. Ed. 0 (2013), (Ed. ). DoD Components reserve a royalty-free, nonexclusive and irrevocable right to reproduce, publish, or otherwise use the work for Federal purposes, and to authorize others to do so (DODGARS §32.36). The views, opinions and/or findings contained in this report are those of the author(s) and should not be construed as an official Department of the Army position, policy or decision, unless so designated by other documentation.

Approved for public release; distribution is unlimited.

# A COMBINED FINITE-ELEMENT/DISCRETE-PARTICLE ANALYSIS OF A SIDE-VENT-CHANNEL-BASED CONCEPT FOR IMPROVED BLAST-SURVIVABILITY OF LIGHT TACTICAL VEHICLES

**M. Grujicic, R. Yavari, J. S. Snipes, S.Ramaswami**

Department of Mechanical Engineering  
Clemson University, Clemson SC 29634

**R. Gupta**

Army Research Laboratory – Survivability Materials Branch  
Blast Protection Branch, Protection Division  
Aberdeen, Proving Ground, MD 21005-5066

Correspondence to: <sup>1</sup>

Mica Grujicic, 241 Engineering Innovation Building, Clemson University, Clemson, SC 29634-0921;  
Phone: (864) 656-5639, Fax: (864) 656-4435, E-mail: [gmica@clemson.edu](mailto:gmica@clemson.edu)

## ABSTRACT

The recently proposed concept solution for improving blast-survivability of the light tactical military vehicles is critically assessed using combined finite-element/discrete-particle computational methods and tools. The proposed concept involves the use of side-vent-channels attached to the V-shaped vehicle underbody. Since the solution does not connect the bottom and the roof or pass through the cabin of a light tactical vehicle, this solution is not expected to: (a) reduce the available cabin space; (b) interfere with the vehicle occupants' ability to scout the surroundings; and (c) compromise the vehicle's off-road structural durability/reliability. Furthermore, the concept solution attempts to exploit ideas and principles of operation of the so-called "*pulse detonation*" rocket engines in order to create a downward thrust on the targeted vehicle. To maximize the downward thrust effects and minimize the extent of vehicle upward movement, standard engineering-optimization methods and tools are employed

---

Keywords: Detonation of Shallow Buried Mines, Blast and Soil Ejecta Loading, Discrete-Particle Approach

for the design of side-vent-channels. The results obtained confirmed the beneficial effects of the side-vent-channels in reducing the blast momentum, although the extent of these effects is relatively small (3–4%).

## I. INTRODUCTION

In the present work, the recently proposed side-vent-channel-based blast-mitigation concept [1] for increasing soil-buried mine-blast survivability of light tactical vehicles (e.g. the High Mobility Multipurpose Wheeled Vehicle, HMMWV) has been investigated using a combined finite-element/discrete-particle computational analysis. Hence, the main topics to be overviewed in this introductory section of the present manuscript include: (a) main limitations of the (light) tactical vehicles currently in use; (b) detonation of shallow-buried mines; (c) impulse loading resulting from the interaction of soil ejecta and gaseous detonation products with a target structure; and (d) the side-vent-channel blast-mitigation concept. As far as a review of the computational methods used in the analysis of various mine-blast scenarios is concerned, it will be presented in Section II.

*Limitations of the Current Tactical Vehicles:* The HMMWV is the prototypical light tactical vehicle used by the US military. This vehicle was designed/developed during the Cold War and, not surprisingly, has been found lacking the necessary blast and ballistic resistance in the recent and the ongoing asymmetric warfare, in which the distinction between front line combat and transportation convoys has been severely blurred. Thus, in the past conflict in Iraq and the ongoing conflict in Afghanistan, HMMWVs have mostly been replaced by larger, heavier MRAP (Mine Resistant Ambush Protected) vehicles, which have been specifically designed for resistance to IEDs (Improvised Explosive Devices) blast. However, the added mass which plays a key role in the superior IED survivability of the MRAP, also negatively affects other performance aspects of this vehicle. Specifically: (a) tactical utility/mobility of the MRAP is severely compromised relative to that of the HMMWV; (b) diminished maneuverability of the larger vehicle on narrow city streets; (c) poor fuel economy; (d) the MRAP weight exceeds the payload capacity of the CH-47 Chinook helicopter severely affecting its

transportability; and (e) its weight exceeds the load carrying capacity of over 70% of the world's bridges [2] seriously reducing the range of its deployment.

*Detonation of Shallow Buried Mines:* Detonation is a high-rate chemical reaction in which condensed matter explosive is converted into high-pressure, high-temperature expanding gases (commonly referred to as gaseous detonation products). Expansion of the gaseous detonation products against the surrounding medium is associated with exchange of linear momentum and various energy components (e.g. potential, thermal, kinetic, strain, etc.). In the case of detonation of soil-buried land-mines, two extreme scenarios are generally identified: (a) the so-called “*camouflet*” scenario in which the mine depth of burial is so large that the high potential energy of the detonation products is almost exclusively transformed into inelastic and elastic strain energy of the soil as well as into surface energy of fractured soil particles. In this case, attenuation of the detonation-induced shock waves within the soil is so prevalent that no significant blast wave is generated at the air/soil interface and no soil ejection takes place. In addition, gaseous detonation products remain trapped within the soil. Therefore, in the case of camouflet, structures located at or above the ground are not exposed to any significant threat while underground structures in close proximity can be threatened; and (b) the ground-laid mine detonation scenario in which the impulse energy carried by air-borne shock waves and the kinetic energy of the detonation products pose the main threat to an above-the-ground target structure.

In the majority of situations, mines are shallow-buried in soil and, hence, neither of these extreme scenarios is encountered. While blast waves and detonation products still pose a threat to the target structure, the soil ejecta pose a greater threat. Consequently, the detonation of shallow-buried mines is of main concern to the designers and developers of targeted structures with high blast survivability (e.g. vehicle hull). That is the reason that this regime of mine deployment is discussed in greater detail in the remainder of this section.

The shallow-buried mine detonation process can be described in terms of three well defined temporal phases, Figures 1(a)–(f):

(a) The initial phase, which is characterized by the interaction of high-pressure, high-temperature expanding gaseous detonation products with the surrounding soil. Within this phase, one can typically identify three distinct zones within the soil, the sizes of which scale with the mine characteristic dimension (e.g. radius,  $R_e$ ). The innermost zone, commonly referred to as the “*zone of crushing*”, extends ca.  $2R_e$ –  $3R_e$ . Within this zone the pressures and temperatures are so high that the soil melts/evaporates, rendering knowledge of the material constitutive response irrelevant. The intermediate zone extends between ca.  $3R_e$  and  $6R_e$ , and the soil response to detonation-induced shock loading is dominated by irreversible compaction and crushing/fracturing of the soil particles. The outermost zone extends beyond ca.  $6R_e$  and the (attenuated) shock-induced soil response within this zone is dominated by reversible/elastic deformation of the soil. It is generally believed that the initial phase of shallow-buried mine detonation controls the amount of energy available for conversion into soil kinetic energy and, in turn, the extent of threat posed to the targeted structure (e.g. [3]). Furthermore, the magnitude of the energy available for conversion is affected by factors such as mine shape, mine depth-of-burial, soil properties, etc.;

(b) The initial phase ends, and the next phase (commonly known as “*soil-overburden bubble initiation phase*”) begins, at the moment of arrival of the soil-borne shock wave to and the interaction with the soil/air interface. Due to a large shock-impedance mismatch between soil and air, this interaction results in a weak transmitted compressive shock to air and a very strong reflected tensile-shock/release-wave. Under the influence of the tensile-shock/release-wave and the expanding high-pressure detonation products, the soil overburden begins to expand outward, forming (initially) a hemi-spherical dome. This phase typically lasts for a few milliseconds and ends with the moment of rupture of soil overburden and the onset of venting of the detonation products; and

(c) The final phase of shallow-buried mine detonation is characterized by gaseous detonation product venting and pronounced soil ejection. Typically, the soil overburden represents only a minor fraction of the total ejected soil. The remaining major portion of the ejected soil is the result of the erosion of the cavity walls by the swirling gaseous detonation products, still residing within the cavity. This interaction

gives rise to the formation of a soil crater with a volume many times larger than the volume of the detonated charge. The trajectory of the ejected soil falls within an inverted cone with a total included angle of 60–90°. Typically, the included angle varies inversely with DOB and soil initial density.

*Detonation-Induced Impulse Loading Experienced by the Target Structure:* Numerous instances of soldier casualties and tactical vehicle destruction incurred by the U.S. military during the recent/ongoing campaigns in Iraq and Afghanistan have been caused by buried and roadside landmines. Detonation of these landmines produces large impulsive loads on the targeted vehicle/personnel through impact by the resulting blast waves, ejected soil and expanded gaseous detonation products. Development of military vehicles (and general structural platforms) with a high-level of blast-survivability entails: (a) the understanding of and ability to quantify the impulsive loads associated with the detonation of landmines deployed in soil of differing compositions/constitutions; and (b) the ability to predict the kinematic and structural (including failure) response of the targeted platforms. Acquiring such understanding and predictive ability, however, is typically quite challenging since the detonation-induced loads depend strongly on the deployed mine's shape, size and depth of burial (DOB), the distance between the soil surface and the target (the so-called stand-off distance, SOD), and the soil properties (density, particle size and distribution, presence of inorganic/organic matter, water content, etc.).

An examination of the public-domain literature conducted for the present work revealed a number of scientific papers and technical reports pertaining to the problem of detonation of buried (explosive) charges. Most of the reported studies, however, are focused on the investigation of soil cratering processes (with emphasis on the efficient utilization of explosives for excavation) and not on the elucidation of blast phenomena and characterization of landmine blast output or on the survivability of structures subjected to blast-loading [3].

Among the reported experimental studies dealing with mine-detonation loading and kinematic/mechanical response of the targeted structure, the following appear to be the most closely related to the subject matter of the current study: (a) Westine et al. [4]



conducted a series of experiments using a plate fixtured and centered above a (Anti-Tank landmine-simulating) buried charge. The plate was perforated at different radial distances and plugs of known mass were placed in the holes. Under the influence of the mine detonation-induced blast loads, the plugs were forced out of the plate and the local impulsive loading on the plate was quantified by measuring the plug velocity; (b) based on the results of Westine et al. [4], Morris [5] developed a computer code for design of mass-efficient, blast survivable vehicles/structures; (c) in the work of Bergeron et al. [6], an instrumented ballistic pendulum was utilized to investigate mine detonation-induced loads experienced by a target structure. In addition, this work quantified: (i) the time-dependent pressure and impulse at several locations in air directly above the mine; (ii) the time-dependent pressure and impulse at several locations in the sand surrounding the mine; and (iii) x-radiographs and high speed photographs of the associated soil cratering and ejection phenomena; and (d) the work of Bergeron et al. [6] was subsequently extended by Braid [7] who incorporated improved instrumentation along with different charge sizes and soil types.

*The Side-Vent-Channel Blast-Mitigation Concept:* Due to the aforementioned inadequate blast-survivability of the light tactical vehicles, the US military is in constant search of new and effective blast-mitigation concepts which do not compromise vehicle mobility/maneuverability, transportability, deployability or fuel economy. One such concept is the use of V-shaped vehicle hulls. Simple schematics of the two common V-hull-based solutions are provided in Figures 2(a)–(b). The standard V-hull solution is depicted in Figure 2(a). In this case, the blast-mitigation performance increases with an increase in the V-hull steepness. However, constraints associated with vehicle ground clearance and height limit the maximum allowable V-hull steepness. A truncated V-hull design is depicted in Figure 2(b). In this case, depending on the location of the detonated mine or IED, the blast-mitigation performance may be enhanced relative to that offered by the design depicted in Figure 2(a). The origin of this potential enhancement is that the benefits (decreased blast impulse) offered by the increased steepness of the V-hull may outweigh the penalty (i.e. increased blast impulse) incurred due to the small flat section.

In our recent work [1], a new blast-mitigation concept, the so-called side-vent-channel concept, was proposed and investigated computationally. As shown schematically in Figure 3, this concept utilizes side vent tubes/channels (of the appropriate cross-sectional shape and wall thickness) attached to the V-shaped vehicle underbody and open at both ends. The bottom end of each tube is cut parallel to the ground (to promote inflow of the detonation by-products and soil ejecta and to prevent structural collapse, crushing, of the tube inlet under blast loads) and flush with the V-hull bottom. The channels/tubes are intended to function as exhaust nozzles as in the case of the pulse-detonation engine and, thus, provide a downward thrust to the vehicle. The secondary role of the channels/tubes is to reduce the blast momentum transferred to the targeted vehicle by enabling the venting of the gaseous detonation products, soil ejecta and mine-casing fragments. The geometry of the side-vent-channels is optimized with respect to the attainment of the maximum downward thrust on the vehicle by coupling an optimization algorithm with a computational analysis (analogous to the one often employed in the case of design of pulse detonation rocket engines). It should be noted that in order to prevent potential misuse of the ideas proposed and the results obtained in the present work, the term “*vehicle*” has been replaced in Figure 3 as well as in the remainder of the manuscript with the term “*surrogate box structure*” (SBS).

The results obtained in Ref. [1] clearly demonstrated that the side-vent-channels: (i) promote venting of soil ejecta, gaseous detonation products and mine casing fragments resulting from a mine-blast underneath the vehicle (and thus lower the blast impulse transferred to the vehicle); and (ii) help create a downward thrust on the vehicle via the promotion of supersonic expansion of gaseous detonation products exiting the channel (and thus lower the possibility for the vehicle lift-off from the ground). In addition, due to the fact that the side-vent-channels are attached externally to the V-hull, they: (a) do not limit the mobility of the occupants within the vehicle and their ability to survey the surroundings; and (b) do not increase cabin rigidity and, hence, are not expected to compromise vehicle structural reliability and durability (associated with an increased rate of vehicle-frame fatigue-induced failure).

The computational analysis employed in Ref. [1] was of a combined Lagrangian/Eulerian fluid-structure interaction (FSI) type and, hence, suffered from at

least the following two major deficiencies: (a) difficulties in defining the Eulerian material (e.g. detonation products, soil and air) interfaces and Lagrangian/Eulerian contact surfaces; and (b) inability to fully account for the granular nature of the soil ejecta. These deficiencies of the combined Eulerian/Lagrangian analyses employed in the computational investigation of the side-vent-channel concept in Ref. [1] are addressed in the present work.

*Main Objectives:* The main objective of the present work is to address the aforementioned deficiencies of the computational analyses of the side-vent-channel concept reported in Ref. [1] by employing a combined finite-element/discrete-particle computational algorithm. Within this purely Lagrangian algorithm, difficulties associated with the definition of the material surfaces and contact interfaces are avoided while soil (as well as the detonation products and air) is given a discrete-particle character.

*Paper Organization:* A brief description of the problem analyzed in the present work and a brief overview of the computational methods and tools used are provided in Section II. The main results obtained in the current work are presented and discussed in Section III. The main conclusions resulting from the present work are summarized in Section IV.

## **II. PROBLEM DESCRIPTION AND COMPUTATIONAL ANALYSIS**

As mentioned earlier, the main objective of the present work is to re-examine the new side-vent-channels blast-mitigation concept using a novel coupled finite-element/discrete-particle computational analysis. In this section, details are presented regarding the basic problem formulation as well as regarding the computational procedure utilized.

### **II.1 PROBLEM DESCRIPTION**

The basic problem analyzed in the present work involves a prototypical buried-mine detonation event followed by the interaction of gaseous detonation products, soil ejecta and blast waves with the target structure, a mock-up of an SBS equipped with a V-shaped vehicle hull underbody and side-vent-channels. Details regarding the

computational model and the numerical procedure employed in the present work to investigate the blast-mitigation potential of the side-vent-channel concept are presented in subsequent sections.

## II.2 COMPUTATIONAL DOMAIN

The computational domain used consists of two separate sub-domains, one of the continuum Lagrangian-type and the other of a discrete-particle type. The Lagrangian sub-domain comprises the SBS equipped with the V-hull and side channels, and is modeled as a finite-element structure consisting of 61,348 three-noded shell elements. In most of the analyses, the SBS structure is rigidized while in a few other analyses flexibility/deformability and damage/structural failure of the SBS was taken into account. During the vent-channel-geometry optimization, the inlet cross-sectional area and the outlet-to-inlet area ratio were varied.

As far as the discrete-particle sub-domain is concerned, it comprises mine/detonation-products, sand/soil, and the ambient air. The discrete-particle sub-domain is of a rectangular parallelepiped shape which encloses the SBS. Details regarding the discrete-particle modeling and simulations will be presented in the next section.

It should be noted that the SBS structure possesses two vertical planes of symmetry, suggesting that only one-quarter of the computational domain has to be analyzed explicitly. However, due to random distribution of the discrete (detonation-products, soil and air) particles, the entire computational domain was analyzed. By analyzing the entire computational domain, rather than one of its quarters, potential rotation of the SBS is also enabled. Figure 4 shows an initial configuration of the prototypical computational domain analyzed.

## II.3 DISCRETE-PARTICLE FORMULATION

As mentioned above, the behavior of high-explosive (HE) gaseous detonation products, soil and air, following detonation, and during their collision with the SBS is modeled in the present work using the discrete-particle (also known as the “*corpuscular*”) approach proposed recently by Olovsson et al. [8]. Within this approach, HE gaseous detonation products, soil and air are all represented as assemblies of

discrete, rigid, spherical, interacting particles which exchange momentum and kinetic energy during their collisions/contact with each other and/or the SBS. To make the computational cost manageable, each particle is defined to represent a collection of  $10^{15}$ – $10^{20}$  molecules.

As explained by Børvik and co-workers [9, 10], the discrete-particle method has the following three main advantages over the commonly used combined Lagrangian-Eulerian approaches: (a) due to its Lagrangian (material-based) character, the method does not require the calculation of the material advection through the mesh and, hence, does not suffer from errors associated with such calculation; (b) numerical detection and quantification of the contacts and interactions between HE detonation products, soil and air and complex-geometry Lagrangian target structures, which are quite challenging within the combined Lagrangian-Eulerian framework, is greatly simplified and accelerated; and (c) within the same computational model, HE detonation products, soil and air (all modeled using the discrete-particle approach) can be combined with continuum-Lagrangian-type target structures to analyze various scenarios related to detonation of shallow-buried mines and the interactions of the detonation products, soil ejecta and air-borne blast-waves with the structures.

In the remainder of this section, details are presented regarding the discrete-particle models for the HE detonation products, air and soil (with different levels of hydration). It should be noted that, as explained by Olovsson et al. [8], discrete-particle models for the HE detonation products and air are essentially an extension of the kinetic molecular theory of gases, as formulated in 1860 by Maxwell [11]. Specifically: (i) discrete particles used in the numerical model represent a collection of a large number of atoms constituting the material in question; and (ii) inter-particle collisions are assumed to be purely elastic (i.e. kinetic-energy-preserving).

#### *Kinetic Molecular Theory of Gases*

The kinetic molecular theory is a theory which successfully relates molecular-level events such as collisions to the macroscopic properties, e.g. pressure or temperature of an ideal gas. Within the theory, the system of interacting gas molecules is assumed to have the following four properties: (a) the size of the molecules is much

smaller than the average inter-molecular distance. Consequently, the volume of the molecules is negligible in comparison to the volume of the space within which the gas resides; (b) the system is in the state of thermodynamic equilibrium, i.e. there is no net flux of mass, linear momentum or energy through the system; (c) particle dynamics is governed by Newton's laws of motion; and (d) inter-molecular and molecule/structure interactions are perfectly elastic and, thus, not only the linear momentum but also the total kinetic energy is preserved.

The kinetic molecular theory was originally proposed by Bernoulli [12, 13] and further developed by Maxwell [11]. By carrying out a detailed statistical analysis of molecular-level interactions, Maxwell was able to derive the following (often referred to as the Maxwell-Boltzmann) expression for the equilibrium molecular velocity distribution function,  $f(v)$ :

$$f(v) = 4\pi \left( \frac{M}{2\pi RT} \right)^{3/2} v^2 \exp\left( \frac{-Mv^2}{2RT} \right) \quad (1)$$

where  $M$  is the molar mass,  $R$  is the universal gas constant and  $T$  is the absolute temperature.

Based on Eq. (1), Maxwell derived the root-mean-square (rms) molecular velocity,  $v_{rms}$ , as:

$$v_{rms} = \sqrt{\int_0^\infty v^2 f(v) dv} = \sqrt{\frac{3RT}{M}} \quad (2)$$

Under a condition that the gas molecules, modeled as spherical particles, possess a finite radius  $r_p$ , additional important quantities characterizing molecular-level interactions within an ideal gas include the mean-free-path,  $l$ , and frequency of collisions,  $f_c$ , defined as:

$$l = \frac{1}{\sqrt{2} \pi n r_p^2} \quad (3)$$

and

$$f_c = n r_p^2 \sqrt{\frac{8\pi RT}{M}} \quad (4)$$

where  $n$  is the number of molecules per unit volume.

Within the kinetic molecular theory of gases, the pressure is the result of the collisions of the molecules with the surroundings. By computing an average rate of change of the momentum per unit area of the surroundings, Maxwell was able to derive the following expression for pressure,  $p$ :

$$p = \frac{2}{3} e_t = \frac{m}{3V} \sum_{i=1}^N v_i^2 = \frac{mN}{3V} v_{rms}^2 \quad (5)$$

where  $e_t$  is the translational kinetic energy per unit volume,  $m$  is the molecular mass,  $V$  is the volume of the system and  $N$  is the number of molecules in the system.

#### *High-Explosive Gaseous Detonation Products*

The constitutive and the dynamic response of HE gaseous detonation products is represented using the discrete-particle material model proposed by Olovsson et al. [8]. Since a detailed overview of this model could be found in Ref. [8], only a brief account of it is given below. Complete parameterization of the HE discrete-particle model requires specification of the following four quantities: (i) initial mass density,  $\rho_{0,HE}$ ; (ii) initial volumetric internal energy density,  $E_{0,HE}$ ; (iii) constant-pressure to constant-volume heat-capacity ratio  $\gamma_{HE} = C_{p,HE}/C_{v,HE}$ ; and (iv) fraction of the total volume occupied by the discrete particles,  $b_{HE}$ . The four parameters are used to set up a discrete-particle computational model in the following way: (a) once the number of molecules per particle  $N_{mpp}$  is selected,  $\rho_{0,HE}$  is used to determine the number of particles in the computational volume  $N_p$ ; (b) since  $\gamma_{HE}$  controls partitioning of the total specific kinetic energy ( $E_{0,HE} / V = e_{t,HE} + e_{s,HE}$ ) into its translational,  $e_{t,HE}$ , and rotational/vibrational,  $e_{s,HE}$ , components as:

$$\frac{e_{s,HE}}{e_{t,HE}} = \frac{5 - 3\gamma_{HE}}{3\gamma_{HE} - 3} \quad (6)$$

$e_{t,HE}$  and  $e_{s,HE}$  could be determined from the given  $E_{0,HE}$  and  $\gamma_{HE}$  for a system of a given volume  $V$ ; and (c) the extent of the so-called “*co-volume*” effect (discussed below) is controlled by the magnitude of  $b_{HE}$ .

Børvik et al. [10] pointed out that the kinetic molecular theory-based expression for pressure, Eq. (5), typically under-predicts pressure levels at extremely high densities encountered in HE detonation products. The reason for this breakdown is the fact that at such high density levels, the volume of the molecules (the so-called “*co-volume*” effects) could not be neglected (as is done in the case of the kinetic molecular theory). To account for the co-volume effects [14, 15], the radius/size of the HE discrete particles is adaptively increased within the present computational approach. This correction is similar to the van der Waals co-volume correction of the ideal gas pressure, Eq. (5), which involves division of the right-hand side of Eq. (5) by a factor  $(1 - b_{HE})$ . In addition to the aforementioned inability of the kinetic molecular theory to accurately predict pressure at high densities, this theory also fails to account for the experimentally observed sharp drop in pressure during adiabatic expansion of the HE detonation products. To overcome this problem, Olovsson et al. [8] suggested that  $\gamma_{HE}$  be changed from its diatomic ideal-gas value of 7/5 to the monoatomic ideal-gas value of 5/3. It should be noted that both 7/5 and 5/3 values of  $\gamma_{HE}$  are substantially lower than the prototypical empirical values for the HE detonation-product specific-heat ratio (2.7–3.0). These discrepancies arise from the differences in the behaviors of ideal and real gases, and will be addressed in our future communications.

The effect of adiabatic expansion from state 1 to state 2 is described by the following ideal gas relation:

$$\frac{p_2}{p_1} = \left( \frac{V_2}{V_1} \right)^{-\gamma} \quad (7)$$

This relation reveals how increasing  $\gamma_{HE}$  from 7/5 to 5/3 increases the rate of adiabatic expansion pressure drop. It should be noted that, as pointed out above,  $\gamma_{HE}$  controls the  $e_{s,HE}/e_{t,HE}$  ratio and according to Eq. (6), for  $\gamma_{HE} = 5/3$  this ratio becomes zero. In other



words, the total internal energy becomes equal to the kinetic/translational energy (i.e. zero rotational/vibrational kinetic energy is assigned to the HE discrete particles).

In order to parameterize the discrete-particle model for the HE, one must first choose the type/grade of HE. In the present work, C-4 high explosive is selected. For the discrete-particle HE model to be considered realistic, it must reproduce some of the basic findings obtained using experimental and/or purely continuum-type computational approaches. Within the continuum framework, the behavior of HE detonation products is commonly represented using the so-called “*equation of state*” (EOS), a function relating the pressure to the material mass-density/specific-volume and mass-based internal-energy-density/temperature. Typically, either the Jones-Wilkins-Lee (JWL) or the ideal gas EOS is used.

As pointed out by Børvik et al. [10], parameterization of the C-4 discrete-particle model can be carried out by stipulating that the aforementioned requirement is fulfilled. Specifically, Børvik et al. [10] systematically varied the C-4 discrete-particle model parameters within an optimization scheme in order to match the experimental (as well as the continuum-level modeling) results of the so-called “*cylinder test*” [16,17]. Within the cylinder test, an oxygen free high conductivity (OFHC) copper pipe is filled with an HE and the explosive is detonated at one end. This causes the formation of a (transverse) detonation wave and its propagation along the length of the pipe. By monitoring the temporal evolution of the pipe radial displacement/velocity and its spatial distribution along the pipe length, properties of the explosives can be determined and quantified as the parameters of the postulated EOS. For example, for C-4 and the assumed JWL EOS in the form:

$$p = A \left( 1 - \frac{\omega}{R_1 V_{HE}} \right) e^{-R_1 V_{HE}} + B \left( 1 - \frac{\omega}{R_2 V_{HE}} \right) e^{-R_2 V_{HE}} + \omega E_{HE} \quad (8)$$

where  $p$  is the pressure,  $V_{HE} = \rho_{HE} / \rho_{0,HE}$ ,  $E_{HE} / V$  is the volumetric internal energy density, there are five JWL EOS material-model parameters ( $A, B, \omega, R_1, R_2$ ). These parameters were determined by Børvik et al. [10] using an optimization algorithm coupled with the combined Lagrangian-Eulerian finite-element analysis of the cylinder test and the experimental cylinder-test data by Souers et al. [16]. A list of the values for these

parameters can be found in Table 1 of Ref. [10]. It should be noted that the experimental data of Souers et al. [16] used in the JWL EOS material-model parameterization procedure extend to a relative volume ratio of about 6 to 7, while a typical value of this quantity associated with SBS-underbody mine-detonation is in excess of 1000. Hence, the use of the JWL EOS at these high relative-volume-ratios is associated with considerable uncertainty.

To parameterize the C-4 discrete-particle material model, Børvik et al. [10] carried out combined finite-element/discrete-particle simulations within which the OFHC pipe is treated as a continuum-Lagrangian finite-element discretized component (modeled using the Johnson-Cook linear-elastic/strain-hardening/rate-dependent/thermally-softenable-plastic constitutive equation [18]) while C-4 is represented as an ensemble of 1,000,000 discrete particles. Next, within an optimization study, the discrete-particle model parameters are varied systematically until the resulting temporal evolutions and spatial distributions of the pipe radial displacement/velocity (caused by the explosive detonation initiated at one end of the pipe) match the same experimental results as those used for parameterization of the C-4 JWL EOS. The procedure employed by Børvik et al. [10] yielded the following C-4 discrete-particle material-model parameters: (i)  $\rho_{0,HE} = 1601 \text{ kg/m}^3$ ; (ii)  $E_{0,HE} / V = 8.7 \text{ GJ/m}^3$ ; (iii)  $\gamma_{HE} = 7/5$ ; and (iv)  $b_{HE} = 0.35$ . It should be noted that the values for  $\rho_{0,HE}$  and  $E_{0,HE} / V$ , as well as the detonation velocity  $D = 8190 \text{ m/s}$ , were taken directly from the JWL-EOS C-4 parameterization carried out by Souers et al. [16]. In other words, parameter-optimization was carried out only for  $\gamma_{HE}$  and  $b_{HE}$ . It should be further noted that the C-4 discrete-particle material-model parameters listed above yield the Chapman-Jouguet pressure (i.e. the peak pressure at the detonation-wave front) of ca. 44 GPa, a value which is approximately 55 % higher than its generally accepted empirical value of ca. 28 GPa.

#### *Air*

Air surrounding the target structure and located above the soil is treated as a diatomic ideal gas initially at the ambient pressure (101.3 kPa) and reference temperature (298 K). Following Børvik et al. [10], the four basic discrete-particle model parameters are assigned the following values: (a)  $\rho_{0,air} = 1.184 \text{ kg/m}^3$ ; (b)  $E_{0,air} / V = 0.25325 \text{ MJ/m}^3$ ; (c)  $\gamma_{air} = 7/5$ ; and (d)  $b_{air} = 0$  (no co-volume effects considered).

Following the same procedure as in the case of HE detonation products, these parameters are used to determine, at the onset of simulation, the number of the air discrete particles and partitioning of the total internal energy into its kinetic translational and kinetic rotational/vibrational parts. It should be noted that in this case,  $e_{s,air}/e_{t,air} = 2/3$  and  $e_{s,air}$  is not zero any longer. However, while in an ideal-gas molecular system,  $e_{s,air}/e_{t,air}$  acquires this equilibrium value only in a statistical sense, within the present discrete-particle model, the ratio is imposed on each individual particle to reduce the computational cost. It should be further noted that, within the present discrete-particle model for air,  $e_{s,air}$  is treated as a scalar variable, i.e. no explicit consideration is given to the rotational/vibrational degrees of freedom of the particles. Since the collision of two air particles is of an elastic character, the momentum and the total kinetic/internal energy are conserved, as well as the  $e_{s,air}/e_{t,air}$  ratio. These conditions are used to determine particle velocities following collision. As far as the collision between an air particle and a movable/deformable structure is concerned, the exchange of the kinetic translational energy between the particle and the structure causes the  $e_{s,air}/e_{t,air}$  ratio to depart from its equilibrium value until the particle in question collides with another particle.

It is important to recognize that the constancy of  $e_{s,air}/e_{t,air}$  ratio corresponds to the assumption of thermal equilibrium within air. This assumption is justified for air prior to detonation. However, upon detonation, linear momentum transfer from the HE detonation products to air causes the air-molecules/discrete-particles to acquire very large values of their kinetic translational energy (i.e. the condition of thermal equilibrium does not hold any longer).

### *Soil*

While the soil is also modeled using a discrete-particle approach, the soil discrete-particle model differs from those used for the HE gaseous detonation products and air in that soil particle collisions are modeled using a penalty rather than an elastic (or, more precisely, kinematic-elastic) collision algorithm. This was done in order to account for the effects such as: (i) soil-particle finite stiffness; (ii) rate-dependent

dissipative/damping nature of the inter-particle collisions; and (iii) the inter-particle frictional effects.

The essential features of the penalty contact used are depicted schematically in Figure 5 which shows a two-particle contact model. Within this model, particle normal interactions are accounted for by a linear spring (with a spring constant  $k$ ) and a linear dashpot (with a damping coefficient  $c$ ) connected in parallel. As far as the tangential interactions are concerned, they are modeled using a linear spring (also of stiffness  $k$ ) and a Coulomb frictional element (which is characterized by a friction coefficient  $\mu$  and which limits the tangential-spring force). It should be noted that soil-particle fracture processes are not considered since they are associated with minor energy absorption/dissipation effects and, hence, are not expected to significantly affect the computational results. Furthermore, it should be noted that the soil-particle stiffness is not accounted for explicitly since the particles are of a rigid type. Rather, through the proper selection of the stiffness constants of the normal and tangential contact springs, particle stiffness is accounted for implicitly.

As in the case of the HE/air discrete-particle models, only the translational degrees of freedom are considered in the case of the soil discrete-particle model (in order to reduce the computational cost). A limited number of computational analyses in which the rotational degrees of freedom were included show that the results obtained are not greatly affected by the inclusion of soil-particle rotations while the computational cost was greatly increased.

In the present work, both the cases of dry and saturated soil/sand are considered. In the remainder of this section, details are presented regarding the discrete-particle model parameterization for the cases of dry and saturated soil.

*Dry Soil:* Dry soil is represented using constant radius rigid spherical particles with the particle-material density of  $2700 \text{ kg/m}^3$  and the initial particle volume fraction of 0.6 (yielding the soil initial density of  $1620 \text{ kg/m}^3$ ). To fill the soil sub-domain with the particles and to parameterize the contact model, the following three-step procedure is used: (i) the soil sub-domain is first assumed to be a three-dimensional array of identical unit cells with the periodic boundary conditions being applied across the faces

of the unit cells. To determine the initial distribution of the soil particles within the unit cell, the number of particles required to attain a volume fraction of 0.6 are placed in the unit cell while ensuring that no inter-particle penetration takes place. An example of a prototypical soil unit cell is displayed in Figure 6; (ii) next, the unit cell is subjected to volumetric compression, and the particle contact stiffness  $k$  and the contact damping coefficient  $c$  are varied in a systematic manner (while holding the inter-particle friction coefficient at a constant level of  $\mu = 0.15$  [19, 20]) until a good match is obtained between the experimentally measured (for prairie sand containing high level of silt and clay) pressure vs. density and the computed pressure vs. density functional relations. More details of this procedure can be found in our recent work [21]. This procedure yielded  $k = 4 \text{ GN/m}$ ,  $c = 0.0 \text{ MN.s/m}$ , and  $\mu = 0.15$ . The hydrostatic pressure within the unit cell is computed by dividing the average force experienced by the unit cell faces by the face surface area; and (iii) the soil sub-domain is constructed by partitioning it into a three-dimensional array of unit cells and filling each cell identically using the particle configuration obtained in (i).

*Saturated Soil:* In the case of saturated soil, water is not modeled explicitly. Instead, its effect on the distribution and the mechanical response of the soil-particle assembly is accounted for implicitly. Specifically: (a) while keeping the soil-particle size uniform and the particle volume fraction ( $= 0.6$ ) the same as in the case of the dry soil, the weight of water is accounted for by increasing the saturated-soil density to  $(0.6 \times 2700) + (0.4 \times 1000) = 2020 \text{ kg/m}^3$  (yielding the saturated soil-particle effective material density of  $2020 / 0.6 = 3367 \text{ kg/m}^3$ ); (b) to account for an increase in the fully-compacted soil density typically observed in saturated soil, increased particle packing (particle volume fraction  $= 0.64$ ) was achieved by allowing  $\pm 2.5\%$  variations in the soil-particle diameter and by taking advantage of the fact that higher densities are obtained in a system containing particles of non-uniform size. Using the same procedure as above, this yielded the saturated-soil density of  $(0.64 \times 2700) + (0.36 \times 1000) = 2088 \text{ kg/m}^3$  and the saturated soil-particle material density of  $2088 / 0.64 = 3262 \text{ kg/m}^3$ ; and (c) inter-particle contact stiffnesses, damping and friction coefficients were adjusted to account

for the effect of water by utilizing the aforementioned procedure [21]. Specifically, the damping coefficient

$$c = 2\xi\sqrt{mk} \quad (9)$$

is adjusted (by varying the damping ratio  $\xi$ , i.e. the ratio of the damping coefficient and the critical damping coefficient) to match the experimental observations [22] that in wet sand, reflection of a compressive shock wave from the soil/air interface does not produce a loose spray of soil particles (an indication of a weaker reflected tensile shock and an increased inter-particle cohesion). This procedure in conjunction with the saturated soil experimental pressure vs. density data [23, 24] yielded  $k = 40$  GN/m,  $\xi = 0.025$  and  $\mu = 0.01$ .

*Selected Discrete-Particle Size-Based Scaling:* While keeping the number of soil particles per unit cell constant, the total number of soil particles in the model can be adjusted by changing the unit cell size. However, it should be noted that the discrete-particle model parameters for soil are particle-/unit-cell-size dependent and, hence, changes in the particle size have to be accompanied by the appropriate changes in the discrete-particle model parameters. Specifically: (a) the particle-particle contact stiffness  $k$  scales (linearly) with the particle-/unit-cell-size or dimensions; and (b) under the assumption that the damping ratio is particle-size independent, the damping coefficient  $c$ , in accordance with Eq. (9), is seen to scale with the squared particle size. It should be noted that while, as stated above, the discrete-particle model parameters for soil are particle-/unit-cell-size dependent, the scaling procedure described above ensures that the mechanical response of the material to static and dynamic loading is effectively particle-unit-cell size independent.

## II.4 COMPUTATIONAL ANALYSIS-TYPE

The mine blast event and the subsequent interactions between the detonation products, soil ejecta and air blasts with the SBS are analyzed computationally using a finite-element/discrete-particle algorithm. It should be noted that both the discrete-particle and the continuum portions of the computational domain are of a Lagrangian character (i.e. the particle geometry and the finite-element mesh are each attached to

the underlying material). Energy dissipation associated with plastic deformation and damage/failure of the SBS is treated as a heat-source. Due to the extremely short duration of the mine-blast detonation event (ca. tens of milliseconds), heat conduction analysis is not carried out. Rather, the purely mechanical analysis is conducted under adiabatic conditions. The effects of local changes in temperature due to adiabatic heating are accounted for through the use of temperature-dependent SBS-material properties.

## II.5 INITIAL CONDITIONS

Prior to the beginning of the computational analysis, the continuum-Lagrange sub-domain is occupied by the SBS, while the respective parts of the discrete-particle sub-domain are filled with HE detonation products, soil and the ambient air. The continuum-Lagrangian SBS sub-domain is assumed to be initially stress-free and stationary.

**Filling of the discrete-particle sub-domains with air, soil and detonation products was done in the following way:** *Air*: for the selected number of air molecules per discrete particle,  $N_{mpp,air}$ , and the known values of  $\rho_{0,air}$  and  $V_{air}$ , the number of air discrete particles,  $N_{p,air}$ , is computed. These particles are placed randomly within the air computational sub-domain. Next, random velocities are initially assigned to the air particles by sampling the Maxwell-Boltzmann distribution function, Eq. (1), with  $M_{air} = 29$  g/mol and  $T_{air} = 298$  K, while ensuring that the  $v_{rms}$  of the air discrete-particle model is identical to that found in the ideal gas, ca. 506 m/s, as modeled by the kinetic molecular theory, Eq. (2). This condition ensures that the discrete-particle air pressure (=101.3 kPa) is consistent with  $E_0 / V = 0.25325$  MJ/m<sup>3</sup> and  $\gamma_{air} = 7/5$ , in accordance with the ideal gas law; *Soil*: As far as the soil sub-domain is concerned, it is constructed, as mentioned earlier, by partitioning it into a three-dimensional array of unit cells and filling each unit cell identically while ensuring that no “penetration” (other than the one caused by gravity) exists between the neighboring particles; and *HE detonation products*: In the case of HE, initially stationary particles of undetonated explosive charge are placed randomly within the HE discrete-particle sub-domain following a procedure identical to that used in the case of air particles. Next, the explosive charge is

detonated. Within the discrete-particle framework, HE detonation is simulated in the following way. At  $t=0$  (the detonation time), with the exception of the HE located at the detonation point(s), the explosive is assumed to be in the solid state and, as mentioned above, the HE discrete particles are assumed to be at rest (more precisely, to have a zero average translational velocity). As the detonation front expands, increasingly more HE is detonated, i.e. converted into the gaseous state due to arrival of the detonation front. Once this solid-gas conversion takes place in a region, the HE particles are assigned a velocity by randomly sampling the Maxwell-Boltzmann thermal velocity distribution function, Eq. (1) [11], consistent with the  $\rho_{C-4} = 1.82 \text{ g/cm}^3$ ,  $M_{C-4} = 222 \text{ g/mol}$  and  $T_{C-4} = \text{ca. } 3500 \text{ K}$ , where detonated C-4 is treated as monoatomically decomposed RDX,  $\text{C}_3\text{H}_6\text{N}_6\text{O}_6$ . The sampled velocities are next corrected by dividing them with  $(1 - b_{C-4})^{1/2}$  in order to account for the aforementioned co-volume-induced pressure increase.

## II.6 BOUNDARY CONDITIONS

Over the portions of the computational-domain external surfaces initially associated with air and soil, an external/ambient pressure of 101.3 kPa is applied so that particles arriving at the boundary and associated with a local pressure exceeding the external pressure are allowed to leave the computational domain. On the other hand, particles which arrive at the external boundary and are associated with a sub-ambient local pressure are reflected back into the domain.

## II.7 CONTACT ALGORITHM(S)

As mentioned earlier, soil/soil particle interactions are modeled using a (viscoelastic/frictional normal/tangential) penalty contact algorithm. On the other hand, HE/HE, air/air, HE/air, soil/HE and soil/air particle interactions are modeled using an elastic/kinematic contact algorithm.

As far as discrete-particle/SBS interactions are concerned, they are modeled using a penalty-contact algorithm. Within this algorithm, contact kinematic constraints are enforced by ensuring that the extent of contact pressure is governed by the local surface penetrations (where the default penalty stiffness parameter is automatically maximized subject to stability limits). As far as the shear stresses are concerned, they



are transferred via a “*slip/stick*” algorithm, that is, shear stresses lower than the frictional shear stress are transferred without interface sliding (otherwise interface sliding takes place). The frictional shear stress is defined by a modified Coulomb law within which there is an upper limit to this quantity (set equal to the shear strength of the continuum-Lagrange SBS sub-domain material). The frictional shear stress is then defined as the smaller of the product between the static/kinetic friction coefficient and the contact pressure, on the one hand, and the Lagrangian sub-domain material shear strength, on the other.

## II.8 MATERIAL MODEL(S)

As mentioned earlier, selected portions of the discrete-particle sub-domain are filled with HE detonation products, soil and air. The constitutive models for these three materials, within the discrete-particle framework, have been presented in Section II.3. It should be recalled that while discrete-particle representation of these three materials is based on rigid particles, material’s deformability has been recovered through the use of the appropriate contact algorithms. As far as the continuum-Lagrangian SBS sub-domain is concerned, it was modeled either as a rigid structure or a deformable structure. In the cases when the SBS was modeled as a rigid structure, the material’s constitutive model is fully-defined by the mass density ( $=7850 \text{ kg/m}^3$ , for steel). When the SBS was modeled as a deformable structure, it was assumed to be made of a conventional AISI 4340 steel whose deformation and failure constitutive response could be represented using the Johnson-Cook material model [25]. A detailed overview of this material model including its AISI 4340 parameterization can be found in our recent work [25, 26].

## II.9 COMPUTATIONAL ALGORITHM

The governing mass, linear momentum and energy conservation equations are solved with a second-order accurate explicit combined finite-element/discrete-particle algorithm. All the calculations in the present work are carried out by combining a general-purpose mathematical program MATLAB [27] with a customized version of YADE (Yet Another Discrete Element), an extensible, open-source discrete-element method (DEM) computer program [28]. MATLAB was used to create the

geometrical/meshed models and Python scripts which control YADE-simulation structure and execution, as well as input/output communications.

## II.10 COMPUTATIONAL ACCURACY, STABILITY AND COST

A standard particle-size and mesh-refinement sensitivity analysis was carried out (the results not shown for brevity) in order to ensure that a convergence of the key results is reached with respect to the further variations of these geometrical/mesh parameters. Due to the conditionally-stable nature of the explicit finite element analysis used, the maximum time increment during each computational step had to be kept lower than the attendant stable time increment. A typical 50 ms computational analysis followed by a detailed post-processing data reduction procedure required on average 24 hours of (wall-clock) time on a 12-core, 3.0 GHz machine with 16 GB of memory.

## III. RESULTS AND DISCUSSION

The three-dimensional combined finite-element/discrete-particle computational model and analysis presented in the previous section are utilized in the present section to reassess the potential of the side channels in lowering the blast momentum/kinetic energy transferred to, and the maximum associated acceleration acquired by, the SBS through the operation of venting and downward-thrust effects. The results obtained are analyzed while comparing them with their combined Eulerian/Lagrangian computational counterparts reported in our recent work [1].

### III.1 SBS CONFIGURATIONS ANALYZED

In order to assess the full blast-mitigation potential of the proposed venting system, three distinct SBS configurations were examined. These configurations are shown in Figures 7(a)–(c). The SBS configuration shown in Figure 7(a) has a V-hull, but no side vent-channels. The V-hulled SBS configuration shown in Figure 7(b) contains constant-radius side vent-channels. The V-hulled SBS configuration shown in Figure 7(c) is very similar to that shown in Figure 7(b) except that the side vent-channels are flared (in their exit section). Comparisons of the corresponding results obtained for the three configurations are used to establish the blast-mitigation effects offered by the presence and geometrical aspects of different components of the SBS structure. Specifically: (a) comparisons of the results obtained using configurations

displayed in Figures 7(a)–(b) enables assessment of the blast-mitigation effects arising from the presence of the (constant-radius) side vent-channels; and (b) comparison of the results obtained using configurations displayed in Figures 7(b)–(c) enables assessment of the additional blast-mitigation effects arising from flaring of the side vent-channels. It should also be noted that the configuration displayed in Figure 7(c), containing a V-hull and flared side-vent-channels, is considered as the baseline SBS configuration in the present work.

### III.2 PROTOTYPICAL RESULTS

The computational analyses employed yielded the results pertaining to the temporal evolution and spatial distribution of various particle-state and continuum-field quantities such as particles' position, (translational and rotational) particle velocities, particle/particle and particle/continuum-structure interaction forces and moments, etc. In addition, results pertaining to the explosive-charge detonation-induced loading experienced by, and the subsequent response of, the SBS structure were obtained. In the remainder of this section, a few prototypical results are presented and discussed.

#### *Material Distribution and Temporal Evolution - SBS Baseline Case*

Spatial distribution of three constituent materials (steel, HE detonation products and soil) at four (2 ms, 4 ms, 6 ms and 8 ms) post-detonation times in the case of the baseline SBS configuration (i.e. the configuration displayed in Figure 7(c), containing a V-hull and flared side-vent channels) is shown in Figures 8(a)–(d). In these and subsequent figures, for improved clarity, air is removed while the detonation-products and soil-particles are displayed as spheres with the soil-particles having a smaller radius. Furthermore, for the same reason, initial positions of the soil and landmine particles are regularized while the SBS structure is shown as a wireframe. Examination of the results displayed in Figures 8(a)–(d), as well as their comparison with the corresponding results (not shown for brevity) for the SBS configuration with the V-hull but no side-vent-channels, established that the presence of side-vent-channels helps guide the flow of the gaseous detonation products and soil-ejecta (as well as air) along the direction parallel with the side of the V-hull. Closer examination of the distribution

of the soil and the detonation products within the side-vent-channels reveals that the channels closest to the mine play the dominant role in the blast-venting process. Furthermore, it is seen that the ejected soil initially retains its cohesion and relatively high density, Figure 8(a), while at later post-detonation times, ejected soil breaks up into non-bonded particles and acquires a low density, Figures 8(c)–(d).

#### *The Effect of SBS Configuration on Post-Detonation Material Distribution*

To further reveal the role of the side-vent-channels in mitigating the effect of buried landmine detonation, material spatial distributions at a fixed (12 ms) post-detonation time are shown, respectively, in Figures 9(a)–(c) for the case of (a) the SBS configuration without channels; (b) the SBS configuration with constant cross-section channels; and (c) the baseline SBS configuration with flared channels. To help interpretation of the results displayed in these figures, a single double-headed arrow is used in each case to denote a vertical distance of the SBS top from a fixed reference elevation. Examination of the results displayed in Figures 9(a)–(c) clearly reveals that the introduction of side vent-channels and their flaring help reduce the momentum transferred to the SBS (as visually quantified by the extent of the SBS liftoff). This finding is the result of the increased venting provided by the (flared) side vent-channels.

#### *Particle-Velocity Spatial Distribution and Temporal Evolution - SBS Baseline Case*

Spatial distribution of the particle and SBS velocities at four (2 ms, 4 ms, 6 ms and 8 ms) post-detonation times in the case of the baseline SBS configuration is shown in Figures 10(a)–(d). Examination of the results displayed in Figures 10(a)–(d) clearly reveals: (a) formation of a “hump” on the top surface of the soil above the detonated mine, Figure 10(a); (b) the onset of formation of a crater within the soil, Figure 10(c)–(d); and (c) non-uniform distribution of the particle velocities over the constant- $z$  section of the channels. The velocity non-uniformity is characterized by smaller particle velocities (indicated by the blue or adjacent spectrum colors) in the portions of the channels closer to the V-hull and higher particle velocities (indicated by the red or adjacent spectrum colors) in the portions of the channels farther away from the V-hull. This finding can be rationalized as follows. Interaction of the ejected particles with the portions of the channel walls which are adjacent to the V-hull gives rise to a transfer of

upward momentum to the SBS and an associated reduction in the particle (upward) velocities. On the other hand, interaction of the ejected particles with the portions of the channel walls which are away from the V-hull gives rise to a transfer of a downward momentum to the SBS and the associated increase in the particle (upward) velocities.

#### *The Effect of SBS Configuration on Post-Detonation Particle-Velocity Distribution*

To further reveal the role of the side-vent-channels in mitigating the effect of buried-landmine detonation, velocity spatial distributions at a fixed (12 ms) post-detonation time are shown, respectively, in Figures 11(a)–(c) for the case of (a) the SBS configuration without channels; (b) the SBS configuration with constant cross-section channels; and (c) the baseline SBS configuration with flared channels. Examination of the results displayed in Figures 11(a)–(c) clearly reveals that the introduction of side-vent-channels and their flaring help reduce the (color-coded) vertical velocity of the SBS. It should be noted that the SBS mass is not constant for the three configurations analyzed in Figures 11(a)–(c). Rather, the mass of the configurations displayed in Figures 11(b)–(c) increases by 1.1% and 1.3% respectively, relative to the mass of the SBS configuration displayed in Figure 11(a). Due to this increase in the SBS mass with the introduction of side-vent-channels and their flaring, one cannot directly determine using the results displayed in Figures 11(a)–(c) if the accompanying reduction in the SBS vertical velocity is simply the effect of the increased SBS mass, or the result of a lower transferred momentum. To resolve this problem, the (quantitative) results associated with the SBS vertical velocity displayed in Figures 11(a)–(c) are combined with the corresponding SBS mass to compute the associated transferred momentum. It is found that the transferred momentum is also lowered by the introduction of the side-vent-channels and their flaring (more quantitative analysis of the effect of the SBS configuration on the transferred momentum is presented in Section III.3).

#### *The Effect of SBS Deformability*

All the results presented so far pertain to various cases of rigid SBSs. While the present computational model and simulations enable the inclusion of a deformable SBS, a detailed examination of the effect of the SBS deformability is beyond the scope of the work described in the present manuscript. This topic will be undertaken in our future

communication. Nevertheless, in this section we show one of the results that can be obtained by incorporating SBS deformability. Temporal evolutions of the SBS steel material and the associated von Mises stress at four (2 ms, 4 ms, 6 ms and 8 ms) post-detonation times are shown respectively in Figures 12(a)–(d). For clarity, discrete particles of the gaseous detonation products, soil and air are not shown in these figures. It is seen that, as a result of the interaction between the gaseous detonation products and soil ejecta with the SBS, the SBS in general and the side-vent-channels, in particular, can undergo severe permanent deformation/distortion and damage/fracture. These phenomena are found to negatively affect the extent of momentum transfer to the SBS and the blast-mitigation efficiency of the side-vent-channel concept and, as mentioned earlier, will be the subject of our future communication.

### III.3 BLAST-MITIGATION EFFICIENCY OF THE VENT-CHANNEL CONCEPT

The results presented in the previous section suggested that the presence of flared side-vent channels may have a positive role in reducing the effect of buried-landmine detonation on the SBS. In this section, more quantitative results pertaining to this blast-mitigation effect of the side-vent channels are presented and discussed.

#### *SBS Velocity and Acceleration Temporal Evolution*

Examples of the typical SBS velocity vs. time and SBS acceleration vs. time results obtained in the present work are shown in Figures 13(a)–(b), respectively. In both cases, the quantity plotted along the y-axis is normalized by its maximum value while the time is normalized by its value corresponding to the SBS maximum velocity. Examination of the results displayed in these figures shows that the SBS velocity initially experiences a sharp rise, reaches a peak value and then gradually decreases under the influence of gravity. As far as acceleration is concerned, it reaches its peak value much earlier than the velocity and then sharply drops as the additional momentum transfer to the SBS from the detonation products and soil ejecta decreases.

It should be noted that the (non-normalized) results corresponding to the ones displayed in Figures 13(a)–(b) are used within a flared-channel design-optimization analysis, presented below, to determine the optimal flared-channel size-geometry which maximizes their blast-venting efficiency.

### *Momentum Transfer*

The results of a side-vent-channel design-optimization analysis, in which channel inlet area and the channel inlet-to-outlet area ratio are used as design variables, while the total transferred-momentum percent reduction (relative to the SBS case without side channels) is treated as the objective function (to be maximized), are shown in Figures 14(a)–(b). The results displayed in Figure 14(a) are obtained using the present coupled finite-element/discrete-particle formulation while the ones displayed in Figure 14(b) were obtained using the combined Eulerian-Lagrangian formulation, as originally reported in Ref. [1]. The results displayed as contour plots in these figures reveal that: (a) there is a region in the channel inlet area/channel outlet-to-inlet area ratio design space which is associated with positive reductions in the blast momentum transferred to the SBS; (b) both sets of results, however, indicate that these reductions are relatively small (maximum 3.2–3.5%); and (c) the two sets of results are relatively comparable with each other, with the present coupled finite-element/discrete-particle formulation predicting somewhat larger (3.5% vs. 3.2%) blast-mitigation effects offered by the side-vent flared-channel concept.

It should be noted that, due to the changing geometry and size of the side-vent channels, the SBS mass is not constant within the design space but rather increases both with the channel inlet area and outlet-to-inlet area ratio. Variation of the SBS mass throughout the design space is depicted in Figure 15 using a contour plot. A comparison of the results displayed in Figures 14(a)–(b) with those displayed in Figure 15 reveals that in the portion of the design space in which the transmitted impulse takes on the lowest values, the SBS mass is ca. 9–11% larger than that of the SBS without side channels. This finding is important since an increase in the SBS mass (without any change in the SBS configuration) gives rise to an increase in the magnitude of the transferred momentum. This increase, for the mass of the ejected soil interacting with the SBS, has been estimated to be between 1.5 and 2%. Hence, if the changes in the SBS configuration involving the introduction of side-vent-channels and their flaring can be accomplished without an increase in the SBS mass (e.g. through the use of armor materials with an increased blast efficiency), further reductions in the transferred momentum could be expected.

It should be noted that the results displayed in Figures 14(a)–(b) correspond to the case of a series of rigid SBSs. In the case of a deformable SBS, the results obtained (but not presented for brevity) show that the fluid-structure interaction effects associated with the SBS deformability initially amplify the blast-mitigation effect. However, the overall reduction in the total momentum transferred to the SBS is not significantly lowered in the case when SBS deformability is taken into account.

#### *Kinetic Energy Transfer*

The results of a side-vent channel design-optimization analysis, in which channel inlet area and the channel inlet-to-outlet area ratio are used as design variables, while the total transferred-kinetic-energy percent reduction (relative to the SBS case without side channels) is treated as the objective function (to be maximized), are shown in Figures 16(a)–(b). The results displayed in Figure 16(a) are obtained using the present coupled finite-element/discrete-particle formulation, while the ones displayed in Figure 16(b) were obtained using the combined Eulerian-Lagrangian formulation, as originally reported in Ref. [1]. The results displayed as contour plots in these figures reveal that: (a) there is a region in the channel inlet-area/channel outlet-to-inlet area-ratio design space which is associated with positive reductions in the kinetic energy transferred to the SBS; (b) both sets of results, however, indicate that these reductions are relatively small (maximum 5.1–5.5%); and (c) the two sets of results are relatively comparable with each other, with the present coupled finite-element/discrete-particle formulation predicting somewhat larger (5.5% vs. 5.1%) blast-mitigation effects offered by the side-vent flared-channel concept.

A comparison of the results displayed in Figures 14(a)–(b) and Figures 16(a)–(b) reveals that regions in the design space that contained maximum reductions in the transmitted impulse and maximum reductions in the kinetic energy, nearly coincide. This finding is consistent with the earlier one which confirmed that the transferred momentum reductions were the result of the changes in the SBS configuration, while the associated increase in the SBS mass had a relatively minor effect.

It should be again noted that the results displayed in Figures 16(a)–(b) correspond to the case of a series of rigid SBSs. The corresponding results (not shown



for brevity) obtained for the deformable SBS case show that the overall reduction in the kinetic energy transferred to the SBS, offered by the side-vent channel concept, is not significantly lowered in the case when SBS deformability is taken into account.

### *SBS Acceleration*

It should be first established that SBS acceleration is a key blast-variable which must be monitored/controlled since it is believed to correlate with the extent of occupants' injury. The results of a side-vent-channel design-optimization analysis, in which channel inlet area and the channel inlet-to-outlet area ratio are used as design variables, while the maximum SBS acceleration percent reduction (relative to the SBS case without side channels) is treated as the objective function (to be maximized), are shown in Figures 17(a)–(b). The results displayed in Figure 17(a) are obtained using the present coupled finite-element/discrete-particle formulation while the ones displayed in Figure 17(b) were obtained using the combined Eulerian-Lagrangian formulation, as originally reported in Ref. [1]. The results displayed as contour plots in these figures reveal that: (a) the largest reduction in the maximum SBS acceleration is obtained in the portion of the design space in which both the channel inlet area and channel outlet-to-inlet area ratio acquire the largest values. This finding is consistent with the fact that: (i) the SBS mass also acquires the largest values in this portion of the design space; and (ii) the SBS acquires a maximum acceleration during the earlier inertia-controlled stages of the blast/SBS interaction; (b) both sets of results, however, indicate that these reductions are relatively small (maximum 1.4–1.6%); and (c) the two sets of results are relatively comparable with each other, with the present coupled finite-element/discrete-particle formulation predicting somewhat larger (1.6% vs. 1.4%) blast-mitigation effects offered by the side-vent flared-channel concept.

It should be recognized that a mere increase in the SBS mass results in an acceleration reduction. Since SBS configuration modifications involving the introduction of side-vent-channels and their flaring are accompanied by mass increases, it is important to separate the contributions of the increased mass and the lowered transferred momentum to the observed reductions in the SBS acceleration. Towards that end, the results displayed in Figures 17(a)–(b) are combined with the results

displayed in Figures 15(a)–(b) respectively, in order to determine the percentage reduction in the product of the SBS mass and acceleration, relative to the SBS case without side-vent-channels. It should be noted that this quantity takes on a zero value in the case when the changes in the SBS acceleration are completely controlled by the associated SBS mass changes. The procedure employed showed that additional (but quite small, ca. 0.35–0.4%) maximum-acceleration-reduction effects are obtained in the SBS equipped with flared side-vent-channels of an optimal size/shape. These additional SBS-acceleration reductions are the result of the aforementioned reductions in the SBS transferred momentum.

It should be again noted that the results displayed in Figures 17(a)–(b) correspond to the case of a series of rigid SBSs. The corresponding results (not shown for brevity) obtained for the deformable SBS case show that the overall reduction in the acceleration transferred to the SBS, offered by the side-vent channel concept, is not significantly lowered in the case when SBS deformability is taken into account.

#### **IV. SUMMARY AND CONCLUSIONS**

Based on the results obtained in the present work, the following main summary remarks and conclusions can be drawn:

1. A recently proposed blast-mitigation solution based on the use of flared side-vent channels attached to the V-hull is critically assessed using advanced coupled finite-element/discrete-particle computational methods and tools.

2. In addition to its blast-mitigation role, the proposed solution was found to offer additional benefits, including: (a) it does not compromise the cabin space, ease of movement within the cabin, or ability of the vehicle occupants to scout their surroundings; (b) since it does not alter the key structural layout of the vehicle, it is not expected to degrade the vehicle's (off-road) structural durability/reliability; and (c) the efficacy of the solution is less sensitive to the location of the buried charge underneath the vehicle.

3. To fully assess the blast-mitigation potential of the side-vent channel solution, transient nonlinear-dynamics finite-element/discrete-particle analyses of buried-

landmine detonation and interactions of the soil ejecta, detonation products and air-blast with a target structure is combined with a channel-design optimization analysis.

4. The results obtained show that when the side-vent channels are properly optimized (with respect to their inlet area and outlet-to-inlet area ratio) they can increase the reduction in the total momentum transferred to the target structure (relative to an identical structure without side-vent channels) by up to 3%. As far as the reduction in the maximum acceleration is concerned, it is found to be less sensitive to the design of the side-vent channels, but more sensitive to the overall mass of the target structure. In addition, the acceleration reductions which are purely the result of the changes in the SBS configuration and do not include the associated increase in the SBS mass, are found to be quite small, ca. 0.35–0.4%.

## V. ACKNOWLEDGEMENTS

The material presented in this paper is based on work supported by the Army Research Office (ARO) research contract entitled “*Concept Validation and Optimization for a Vent-based Mine-blast Mitigation System*”, Contract Number W911NF-11-1-0518. The authors want to thank Dr. Frederick Ferguson for his continuing interest and support.

## REFERENCES

1. M. Grujicic, B. d'Entremont, J. S. Snipes, and R. Gupta, "*A Novel Blast-Mitigation Concept for Light Tactical Vehicles*," pending approval from sponsor for manuscript submission, February 2012.
2. J. Capouellez, K. Drotleff, G. Wolfe, A. Cichosz, F. Helsel, A. Mikaila, J. R. Pickens, R. W. Semelsberger, S. Kerr, E. Wettlaufer, P. Massoud, J. Wood and B. Barringer, "*Optimized Light Tactical Vehicle*," 27<sup>th</sup> Army Science Conference, No. FP-11, 2010, 1–8.
3. K. A. Holsapple and K. R. Housen, "*Crater database and scaling tools*," <http://keith.aa.washington.edu/craterdata>, November 2004.
4. P. S. Westine, B. L. Morris, P. A. Cox and E. Polch, "*Development of computer program for floor plate response from land mine explosions*," Contract Report No. 1345, for U.S. Army TACOM Research and Development Center, 1985.
5. B. L. Morris, "*Analysis of Improved Crew Survivability in Light Vehicles Subjected to Mine Blast*," Final Report for Contract No. DAAK70-92-C-0058 for the U.S. Army Belvoir RDEC, Ft. Belvoir, VA, 1993.
6. D. Bergeron, S. Hlady and M. P. Braid, "*Pendulum Techniques to Measure Land Mine Blast Loading*," 17<sup>th</sup> International MABS Symposium, Las Vegas, USA, June 2002.
7. M. P. Braid, "*Experimental Investigation and Analysis of the Effects of Anti-personnel Landmine Blasts*," Defence R&D Canada, Suffield Special Publication, DRES SSSP 2001-188, December 2001.
8. L. Olovsson, A.G. Hanssen, T. Børvik, "*A particle-based approach to close-range blast loading*," *European Journal of Mechanics A/Solids*, 29, 1–6, 2010.
9. T. Børvik, A.G. Hanssen, M. Langseth, L. Olovsson, "*Response of structures to planar blast loads – A finite element engineering approach*," *Computers and Structures*, 87, 507–520, 2009.
10. T. Børvik, L. Olovsson, A.G. Hanssen, K.P. Dharmasena, H. Hansson, H.N.G. Wadley, "*A Discrete Particle Approach to Simulate the Combined Effect of Blast and Sand Impact Loading of Steel Plates*," *Journal of Mechanics and Physics of Solids*, 59, 940–958, 2011.
11. J.C. Maxwell, "*Illustrations of the Dynamical Theory of Gases*," *Philosophical Magazine* 19, 19–32, 1860.
12. D. Bernoulli, "*Hydrodynamica Sive de Viribus et Motibus Fluidorum Commentarii*," Johannis Reinholdi Dulseckeri. Argentorati, Strasbourg, 1738.
13. D. Bernoulli and J. Bernoulli, "*Hydrodynamics*," Dover Publications, 1968.
14. V.F. Baibuz, V.Y. Zitserman, L.M. Golubushkin, I.G. Malyshev, "*The co-volume and equation of state of high-temperature real gases*," *Journal of Engineering Physics and Thermo-physics*, 51, 955–956, 1986.

15. Clausius, R. “Ueber das verhalten der kohlensäure in bezug auf druck, volume und temperature,” *Annalen der Physik und Chemie* 3, 337–357, 1880.
16. P.C. Souers, B. Wu, L.C. Haselman Jr., “Detonation equation of state at LLNL, 1995. Report UCRL-ID119262 Rev 3,” **Energetic Materials Center, Lawrence Livermore National Laboratory, Livermore, CA, USA, 1996.**
17. P.C. Souers, “Cylinder test on C-4. Report UCRL-TR-230845,” **Energetic Materials Center, Lawrence Livermore National Laboratory, Livermore, CA, USA, 2007.** <https://e-reports-ext.llnl.gov/pdf/347222.pdf> [accessed on November 24, 2012]
18. K.J. Frutsky, R.J. Clifton, “High-temperature pressure-shear plate impact experiments on OFHC copper,” *Journal of the Mechanics and Physics of Solids*, 46, 1723–1743, 1998.
19. M. Grujicic, B. Pandurangan, J. D. Summers, B. A. Cheeseman and W. N. Roy, “Application of the Modified Compaction Material Model to Soil with Various Degrees of Water Saturation,” *Shock and Vibration*, 15, 79–99, 2008.
20. M. Grujicic, B. Pandurangan, G. M. Mocko, S.T. Hung, B. A. Cheeseman, W. N. Roy and R. R. Skaggs, “A Combined Multi-Material Euler/Lagrange Computational Analysis of Blast Loading Resulting from Detonation of Buried Landmines”, *Multidiscipline Modeling in Materials and Structures*, 4, 105–124, 2008.
21. M. Grujicic, R. Yavari, J.S. Snipes, S. Ramaswami, “Extension of a Current Continuum-Level Material Model for Soil into the Low-Density Discrete-Particle Regime,” *Journal of Materials Engineering and Performance*, in press. DOI: 10.1007/s11665-012-0429-3
22. V. S. Deshpande, R. M. McMeeking, H. N. G. Wadley and A. G. Evans, “Constitutive Model for Predicting Dynamic Interactions between Soil Ejecta and Structural Panels,” *Journal of Mechanics and Physics of Solids*, 57, 1139–1164, 2009.
23. M. Grujicic, B. Pandurangan and B. A. Cheeseman, “The Effect of Degree of Saturation of Sand on Detonation Phenomena Associated with Shallow-buried and Ground-laid Mines”, *Shock and Vibration*, 13, 41–62, 2006.
24. M. Grujicic, B. Pandurangan, Y. Huang, B. A. Cheeseman, W. N. Roy and R. R. Skaggs, “Impulse Loading Resulting from Shallow Buried Explosives in Water-saturated Sand”, *Journal of Materials: Design and Applications*, 221, 21–35, 2007.
25. M. Grujicic, W. C. Bell, G. Arakere, I. Haque, “Finite Element Analysis of the Effect of Up-armoring on the Off-road Braking and Sharp-turn Performance of a High-Mobility Multi-purpose Wheeled Vehicle (HMMWV)”, *Journal of Automobile Engineering*, 223, D11, 1419–1434, 2009.
26. M. Grujicic, V. Sellappan, M. A. Omar, N. Seyr, A. Obieglo, M. Erdmann and J. Holzleitner, “An Overview of the Polymer-to-Metal Direct-Adhesion Hybrid Technologies for Load-Bearing Automotive Components”, *Journal of Materials Processing Technology*, 197, 363–373, 2008.

27. **MATLAB**, *The Language of Technical Computing*, Version 8.0.0.783, R2012b (The MathWorks Inc., MA).
28. Yade: V. Šmilauer, E. Catalano, B. Chareyre, S. Dorofeenko, J. Duriez, A. Gladky, J. Kozicki, C. Modenese, L. Scholtès, L. Sibille, J. Stránský, and K. Thoeni, Yade Documentation (V. Šmilauer, ed.), The Yade Project, 1st ed., 2010. <http://yade-dem.org/doc/>

## FIGURE CAPTIONS

**Figure 1.** Various phases of detonation of a landmine shallow-buried in soil. Please see text for details.

**Figure 2.** Two blast-mitigation vehicle-hull concepts: (a) V-shaped hull; and (b) truncated V-shaped hull.

**Figure 3.** Side channels/tubes based blast-mitigation concept originally proposed in Ref. [1]. Note that the abbreviation SBS stands for “*surrogate box structure*.”

**Figure 4.** A prototypical computational domain used in the combined three-dimensional finite-element/discrete-particle analysis of the buried-mine detonation event and the subsequent interactions of the detonation products, soil ejecta and air blast with the SBS equipped with a V-hull and side vent channels. Please note that the mine is shallow-buried and its view is obstructed by the surrounding soil.

**Figure 5.** A schematic of the contact-mechanics model involving two interacting equal-sized/mass spherical particles of soil.

**Figure 6.** Prototypical soil unit cell used in the present combined finite-element/discrete-particle computational analysis of mine detonation and interaction of the detonation products, soil ejecta and air blast with the SBS.

**Figure 7.** SBS configurations analyzed in the present work: (a) the plain V-hull configuration; (b) same as (a), but with constant-radius side-vent channels; and (c) same as (b), but with channel flaring.

**Figure 8.** Spatial distribution of soil, HE detonation products and steel used to make SBS in the case of the rigid baseline SBS configuration at post-detonation times of: (a) 2 ms; (b) 4 ms; (c) 6 ms; and (d) 8 ms.

**Figure 9.** Spatial distribution of soil, HE detonation products and steel used to make rigid SBS at a fixed (12 ms) post-detonation time for the case of (a) the SBS configuration without channels; (b) the SBS configuration with constant cross-section channels; and (c) the baseline SBS configuration with flared channels.

**Figure 10.** Spatial distribution of the velocities of the soil and mine-detonation-product particles and rigidized-SBS in the case of the baseline SBS configuration at post-detonation times of: (a) 2 ms; (b) 4 ms; (c) 6 ms; and (d) 8 ms.

**Figure 11.** Spatial distribution of the velocities of the soil and mine-detonation-product particles and rigidized-SBS at a fixed (12 ms) post-detonation time for the case of (a) the SBS configuration without channels; (b) the SBS configuration with constant cross-section channels; and (c) the baseline SBS configuration with flared channels.

**Figure 12.** Temporal evolutions of the SBS steel material and the associated von Mises stress at post-detonation times of: (a) 2 ms; (b) 4 ms; (c) 6 ms; and (d) 8 ms.

**Figure 13.** Examples of the typical: (a) SBS normalized-velocity vs. time; and (b) SBS normalized-acceleration vs. time results obtained in the present work.

**Figure 14.** Percent reduction (relative to the SBS case without side-vent channels) in total blast momentum for the baseline SBS configuration as a function of channel inlet-

area and inlet-to-outlet area ratio: (a) present combined finite-element/discrete-particle analysis; and (b) combined Eulerian/Lagrangian analysis presented in Ref. [1].

**Figure 15.** Percent reduction (relative to the SBS case without side-vent channels) in the mass of the baseline SBS configuration as a function of channel inlet-area and inlet-to-outlet area ratio.

**Figure 16.** Percent reduction (relative to the SBS case without side-vent channels) in total kinetic energy for the baseline SBS configuration as a function of channel inlet-area and inlet-to-outlet area ratio: (a) present combined finite-element/discrete-particle analysis; and (b) combined Eulerian/Lagrangian analysis presented in Ref. [1].

**Figure 17.** Percent reduction (relative to the SBS case without side-vent channels) in maximum acceleration for the baseline SBS configuration as a function of channel inlet-area and inlet-to-outlet area ratio: (a) present combined finite-element/discrete-particle analysis; and (b) combined Eulerian/Lagrangian analysis presented in Ref. [1].



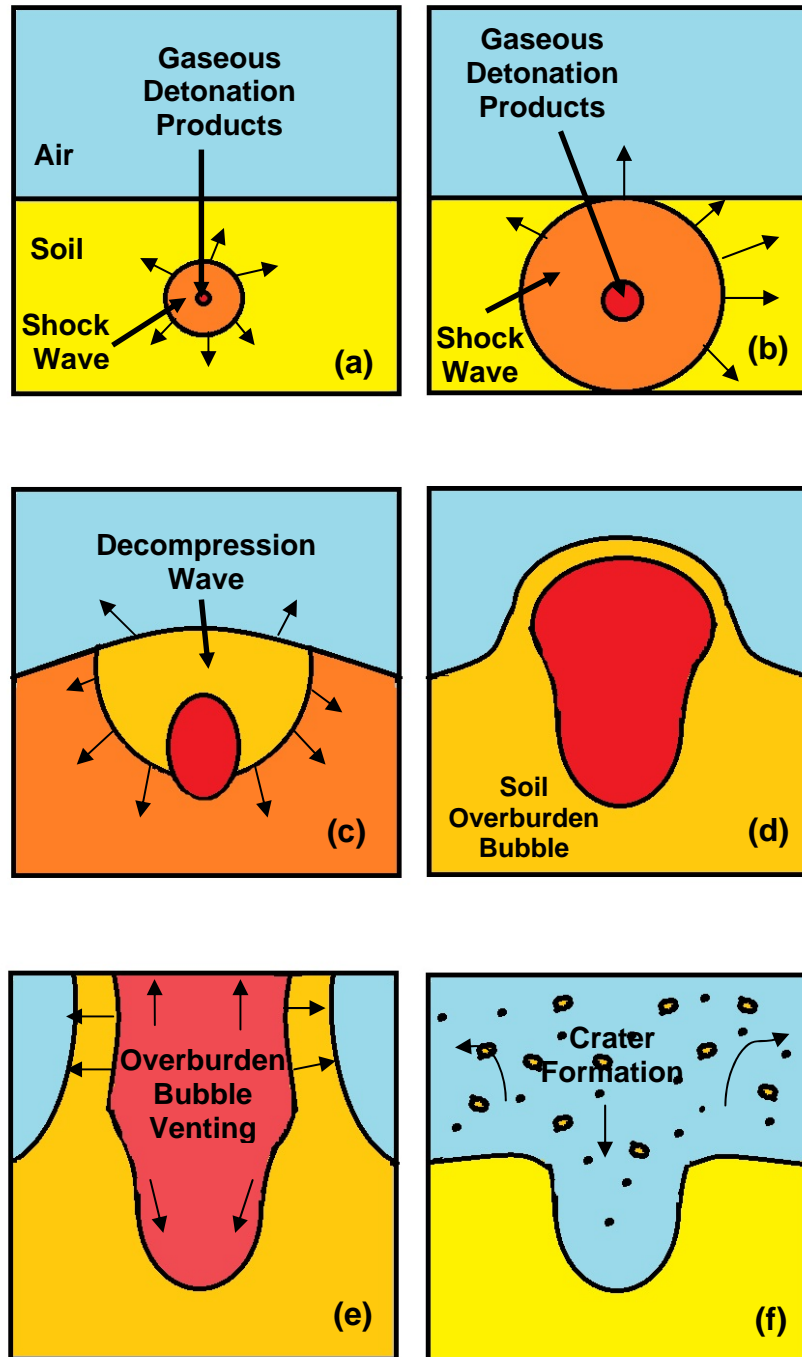


**Figure 1. Various phases of detonation of a landmine shallow-buried in soil. Please see text for details.**

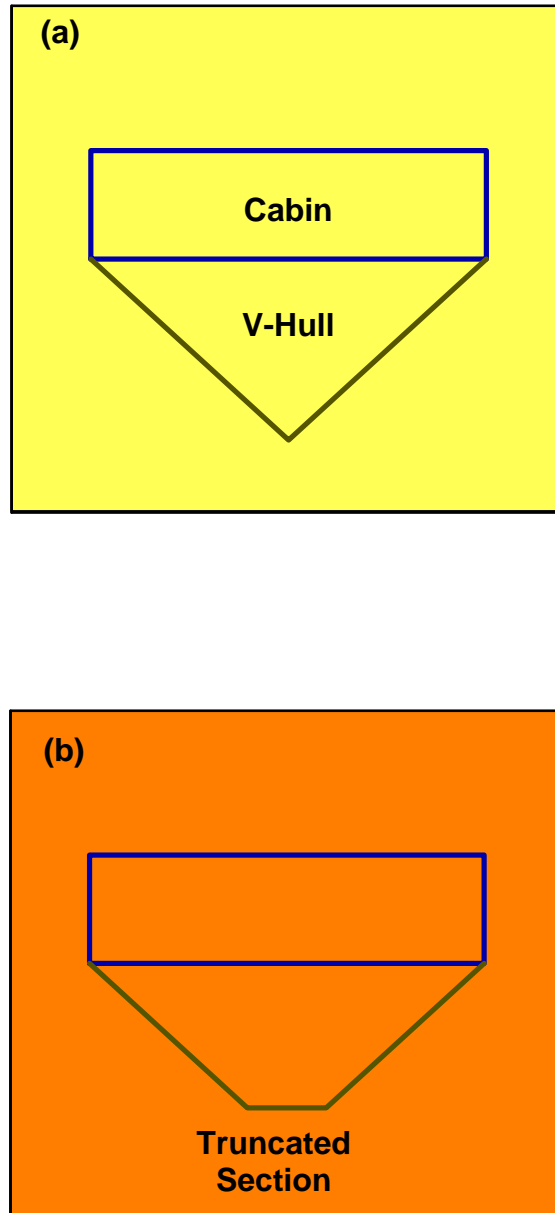


**Figure 2. Two blast-mitigation vehicle-hull concepts: (a) V-shaped hull; and (b) truncated V-shaped hull.**

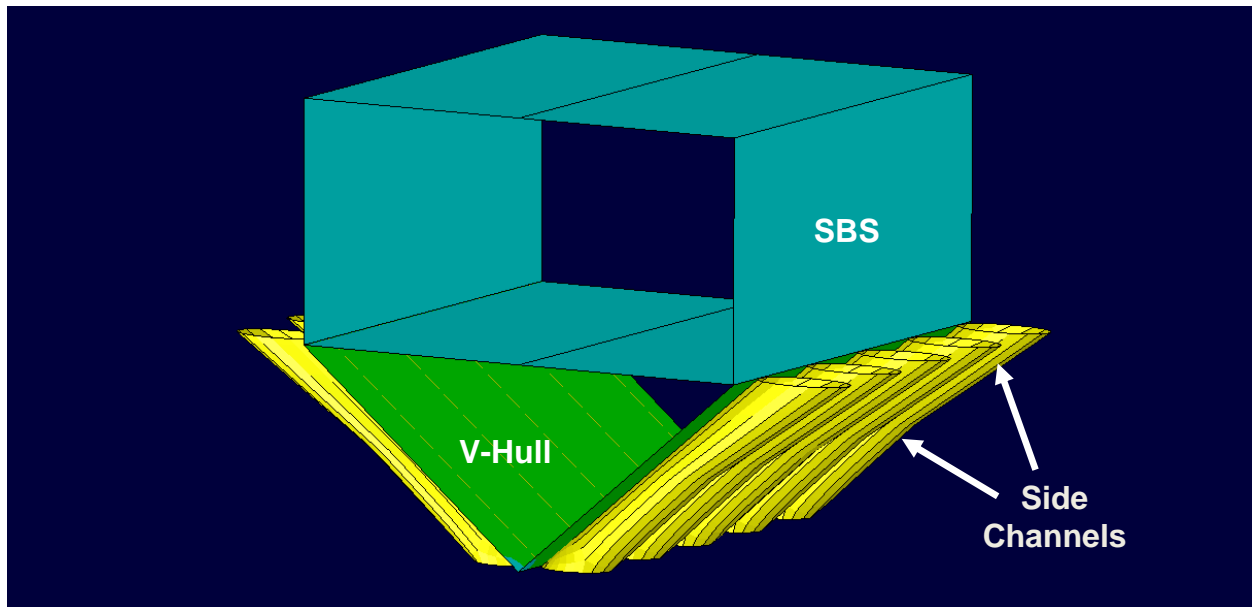


**Figure 3. Side channels/tubes based blast-mitigation concept originally proposed in Ref. [1]. Note that the abbreviation SBS stands for “*surrogate box structure*.”**

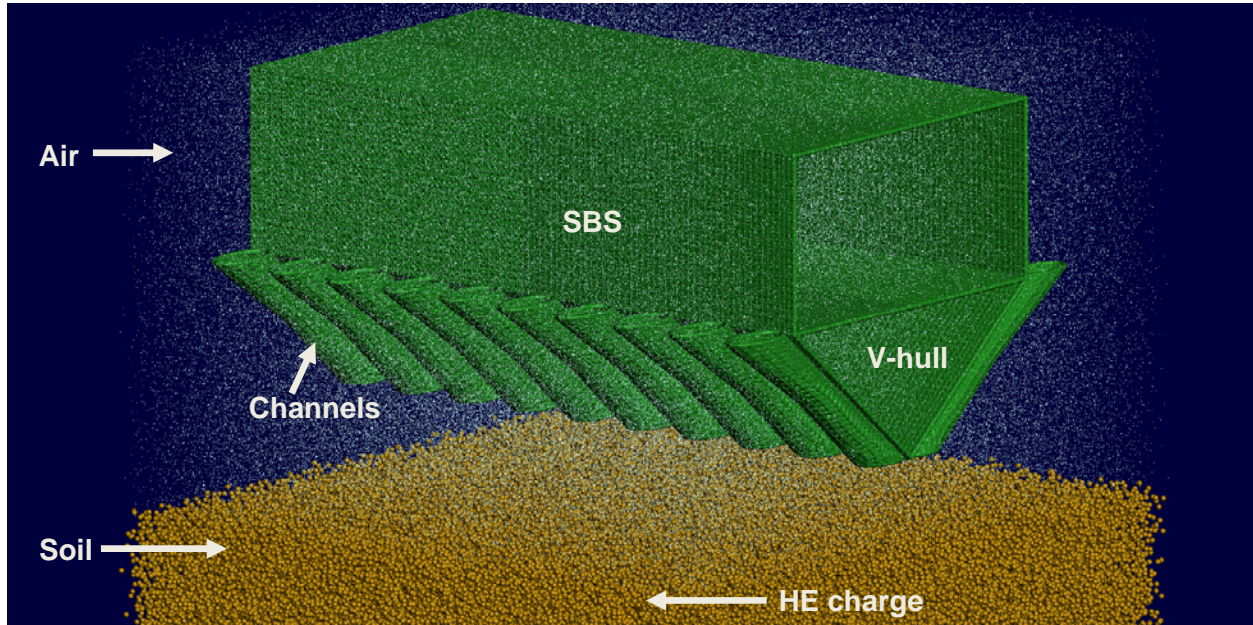


**Figure 4. A prototypical computational domain used in the combined three-dimensional finite-element/discrete-particle analysis of the buried-mine detonation event and the subsequent interactions of the detonation products, soil ejecta and air blast with the SBS equipped with a V-hull and side vent channels. Please note that the mine is shallow-buried and its view is obstructed by the surrounding soil.**

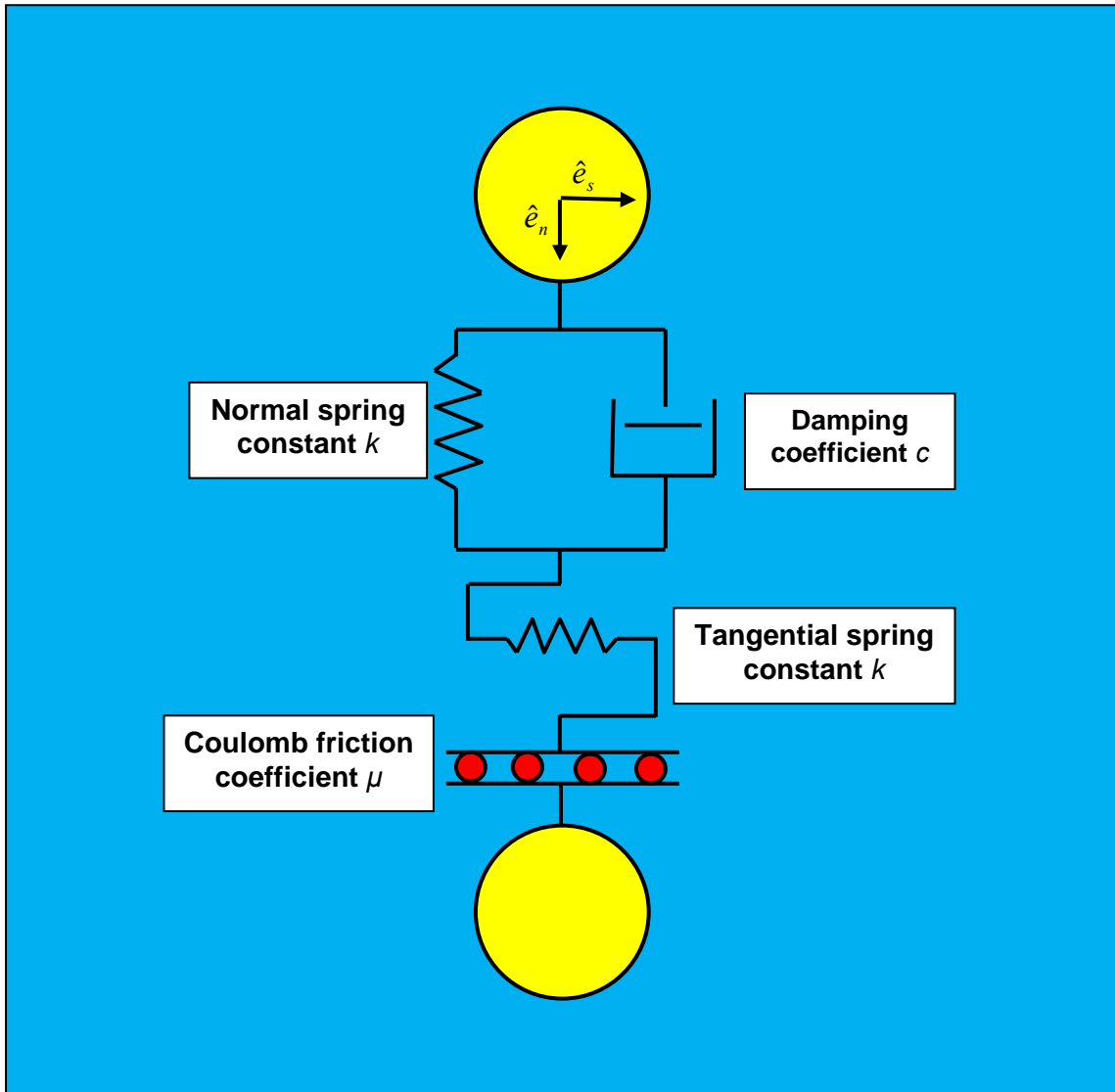


**Figure 5.** A schematic of the contact-mechanics model involving two interacting equal-sized/mass spherical particles of soil.

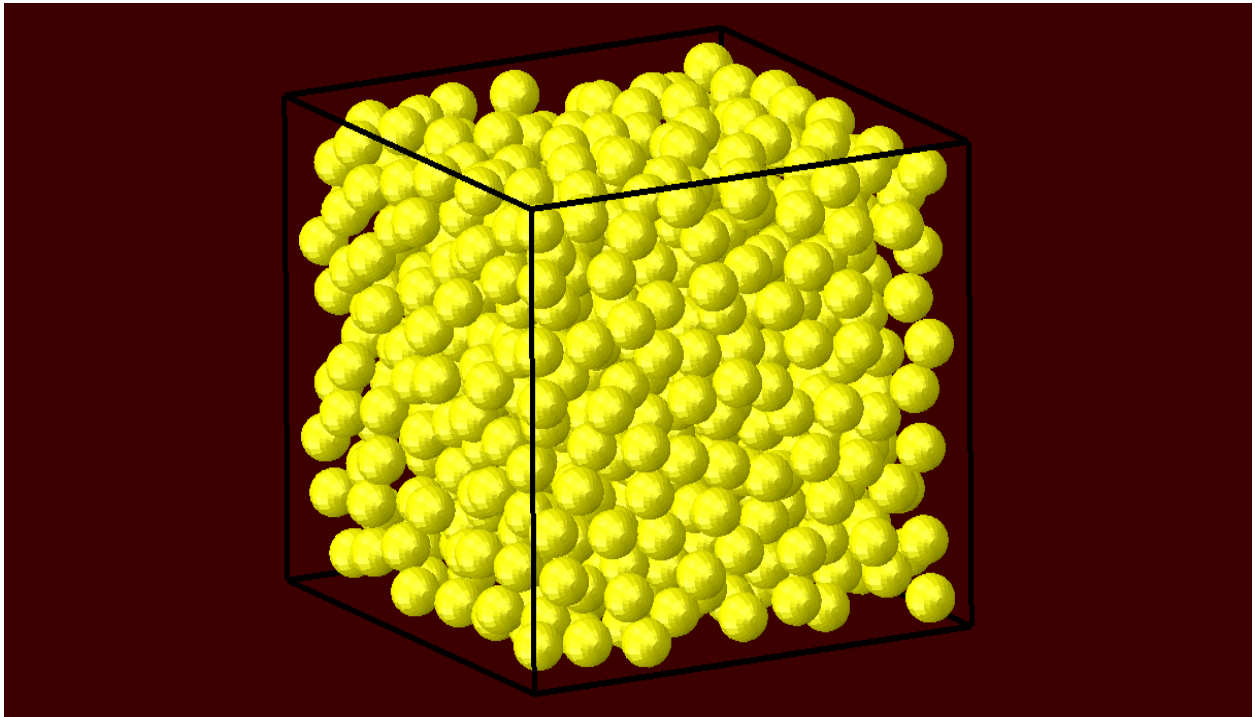


**Figure 6. Prototypical soil unit cell used in the present combined finite-element/discrete-particle computational analysis of mine detonation and interaction of the detonation products, soil ejecta and air blast with the SBS.**

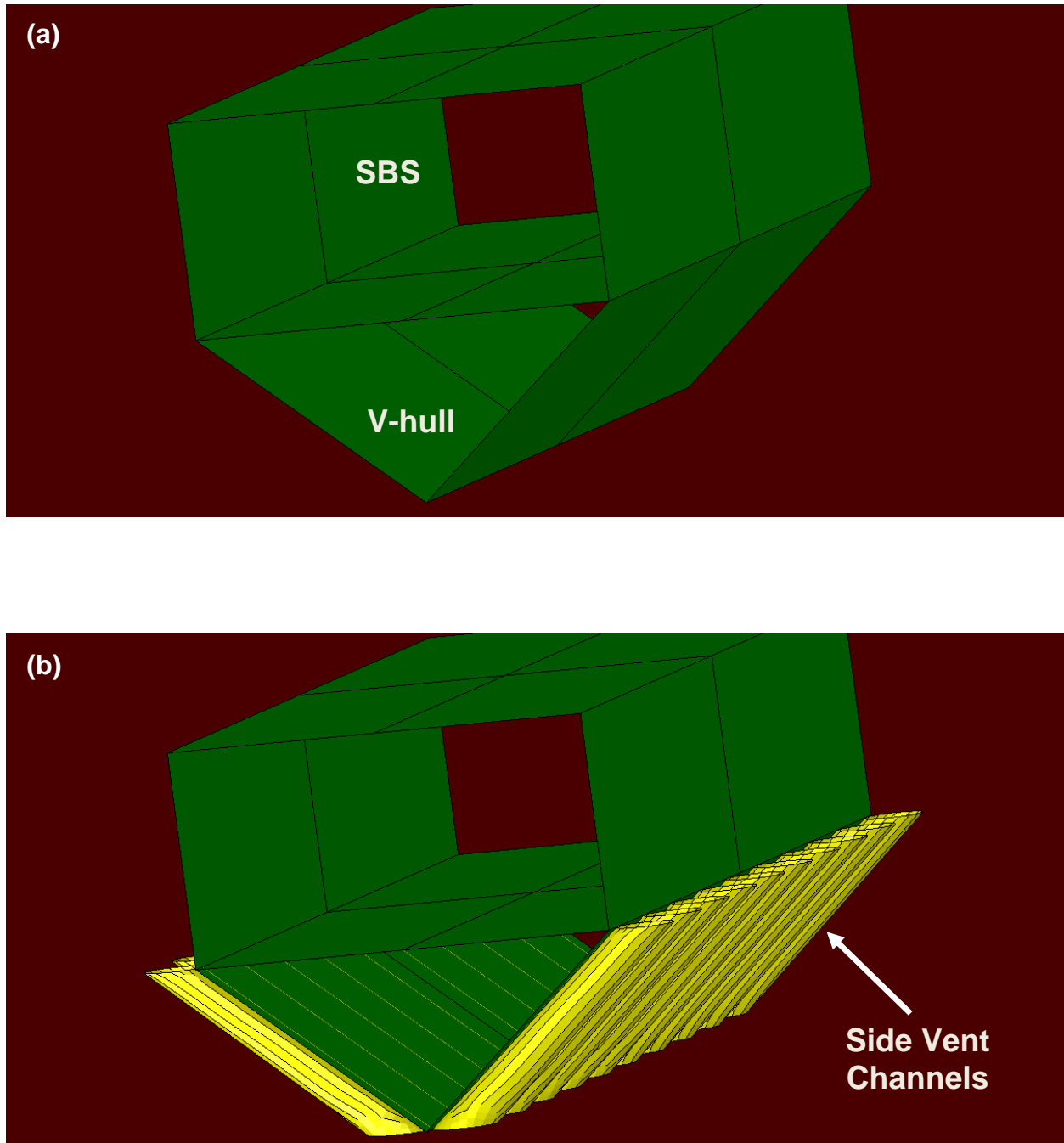


**Figure 7. SBS configurations analyzed in the present work: (a) the plain V-hull configuration; (b) same as (a), but with constant-radius side-vent channels; and (c) same as (b), but with channel flaring.**

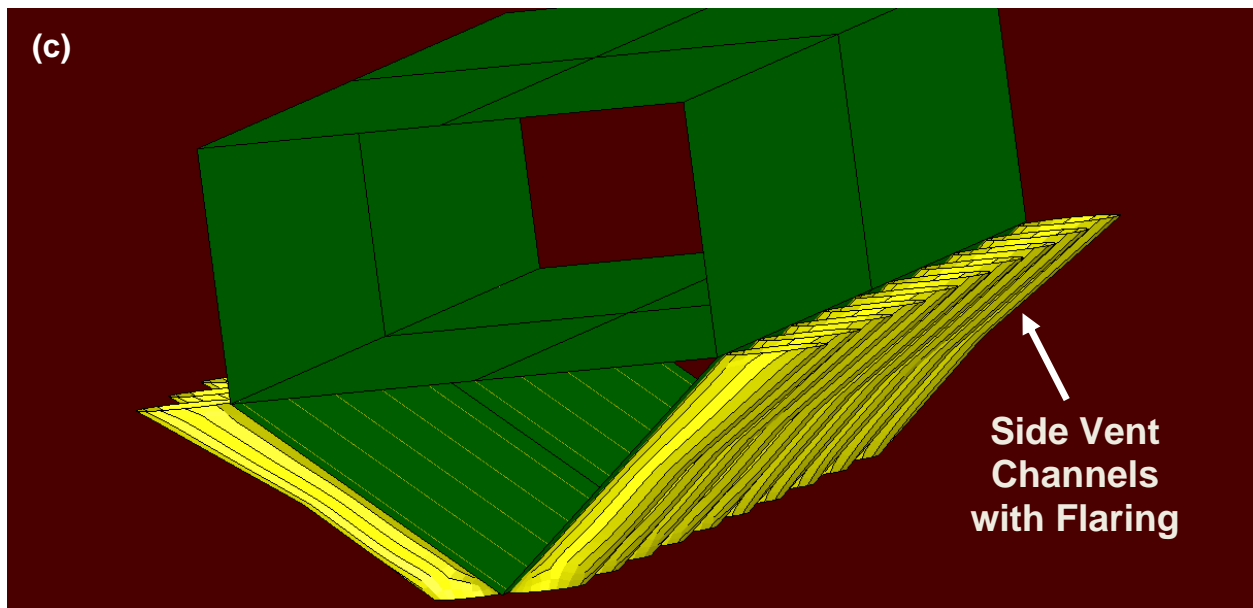


**Figure 7. Continued.**



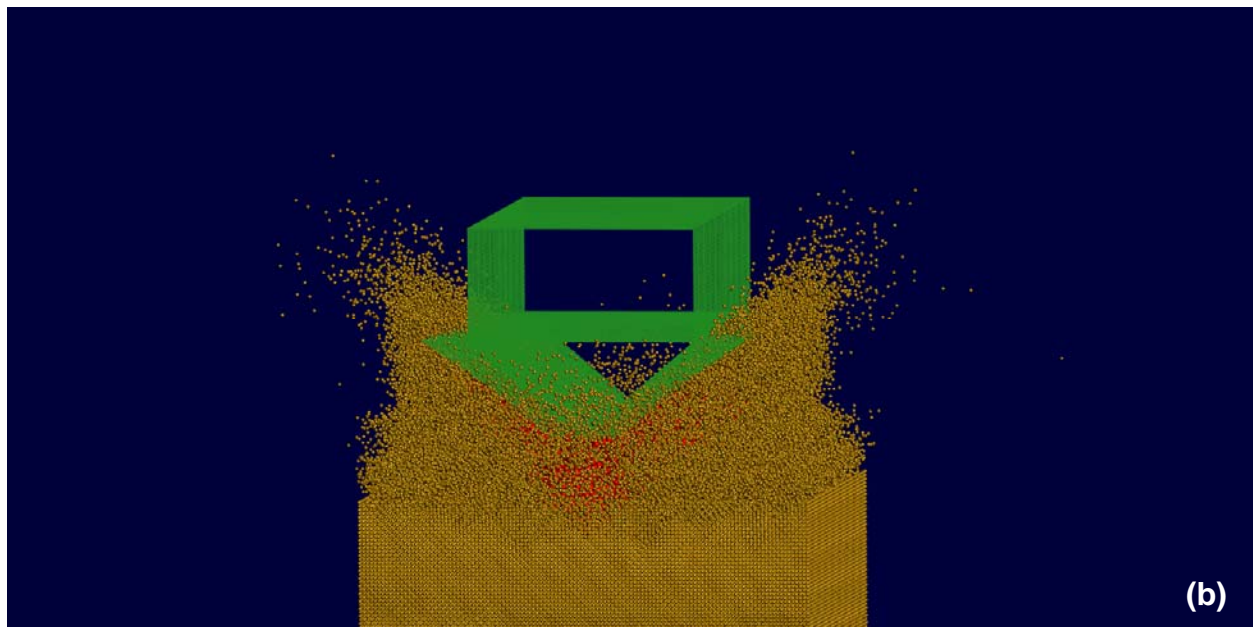
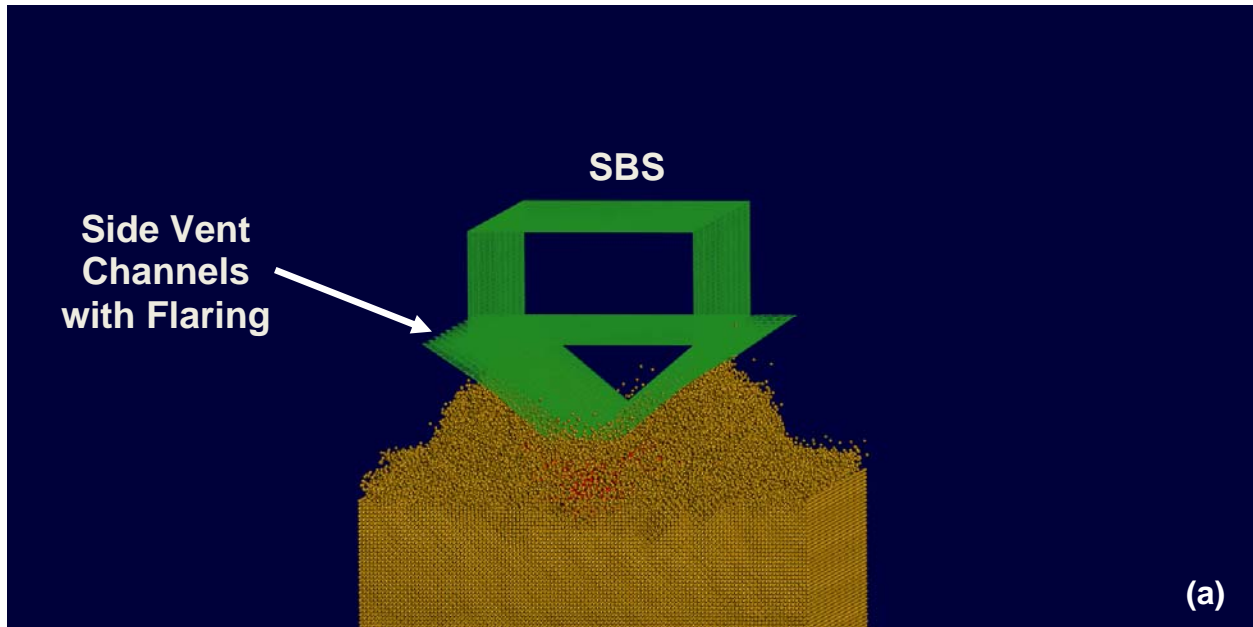


**Figure 8. Spatial distribution of soil, HE detonation products and steel used to make SBS in the case of the rigid baseline SBS configuration at post-detonation times of: (a) 2 ms; (b) 4 ms; (c) 6 ms; and (d) 8 ms.**

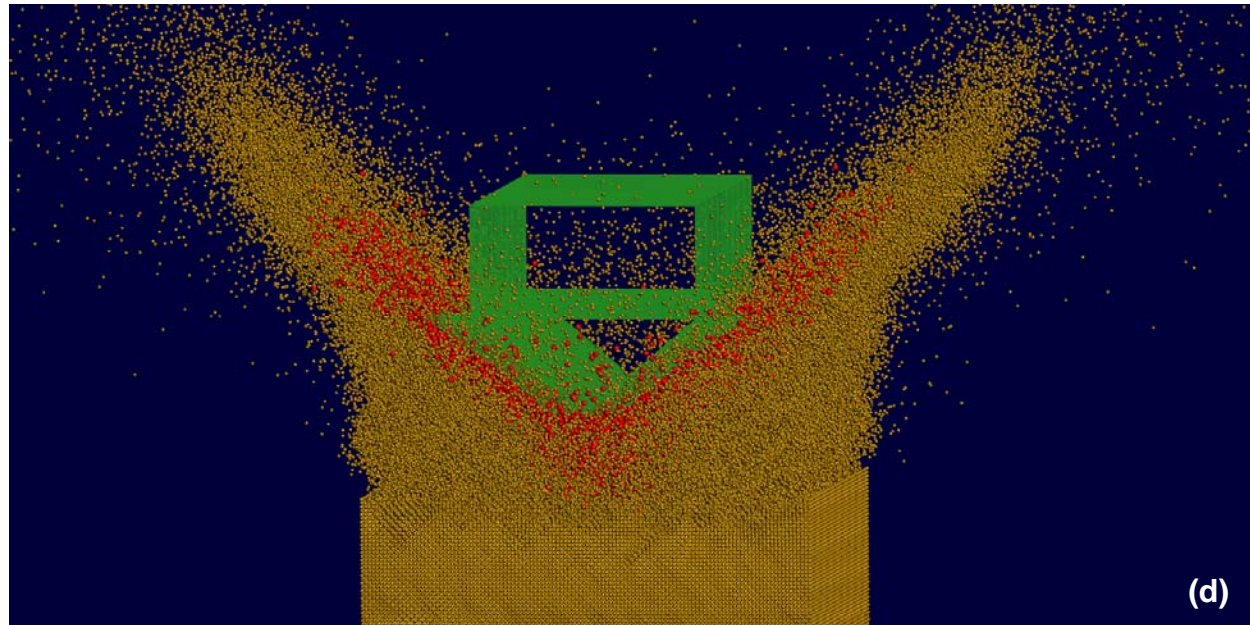
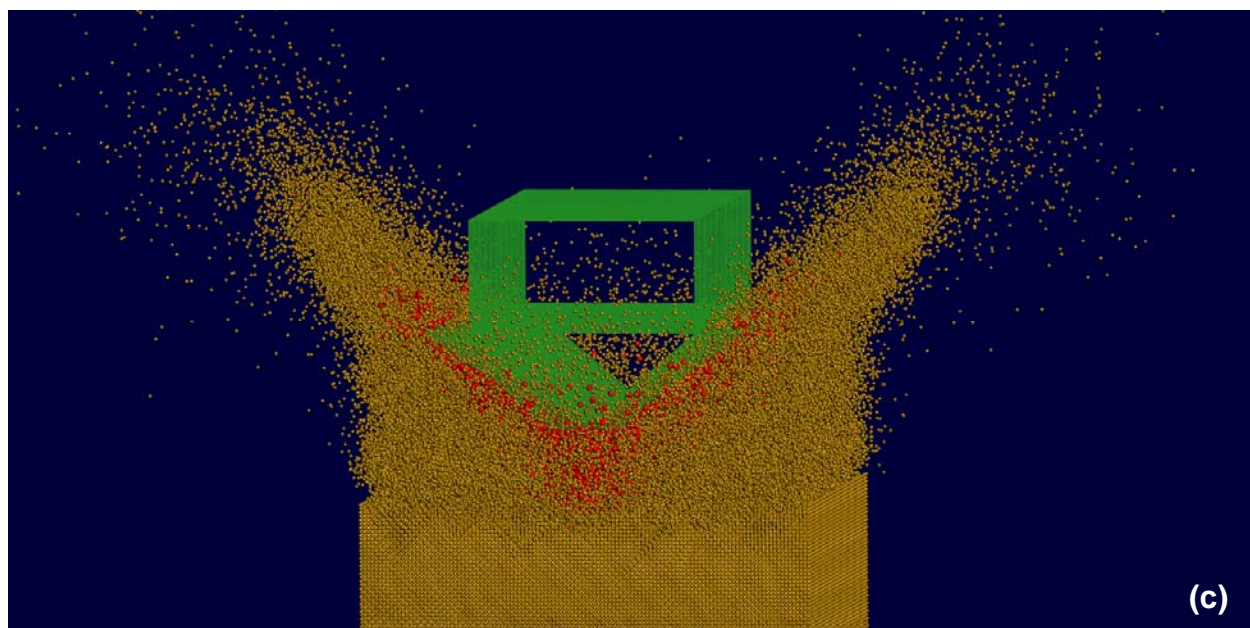


**Figure 8. Continued.**



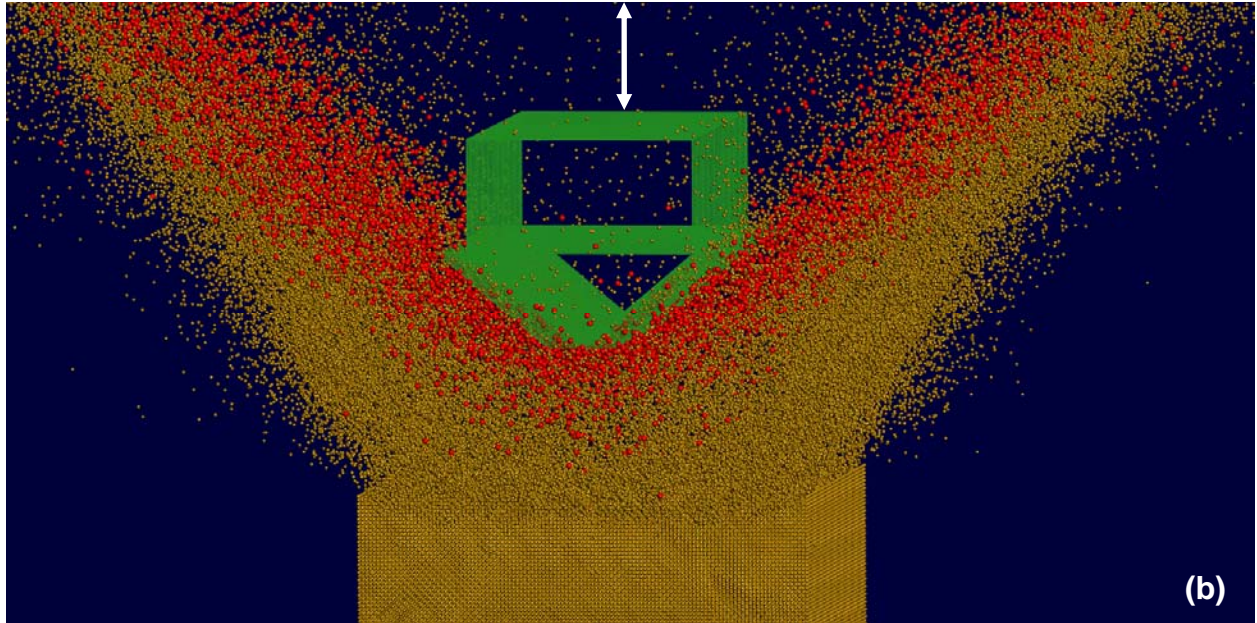
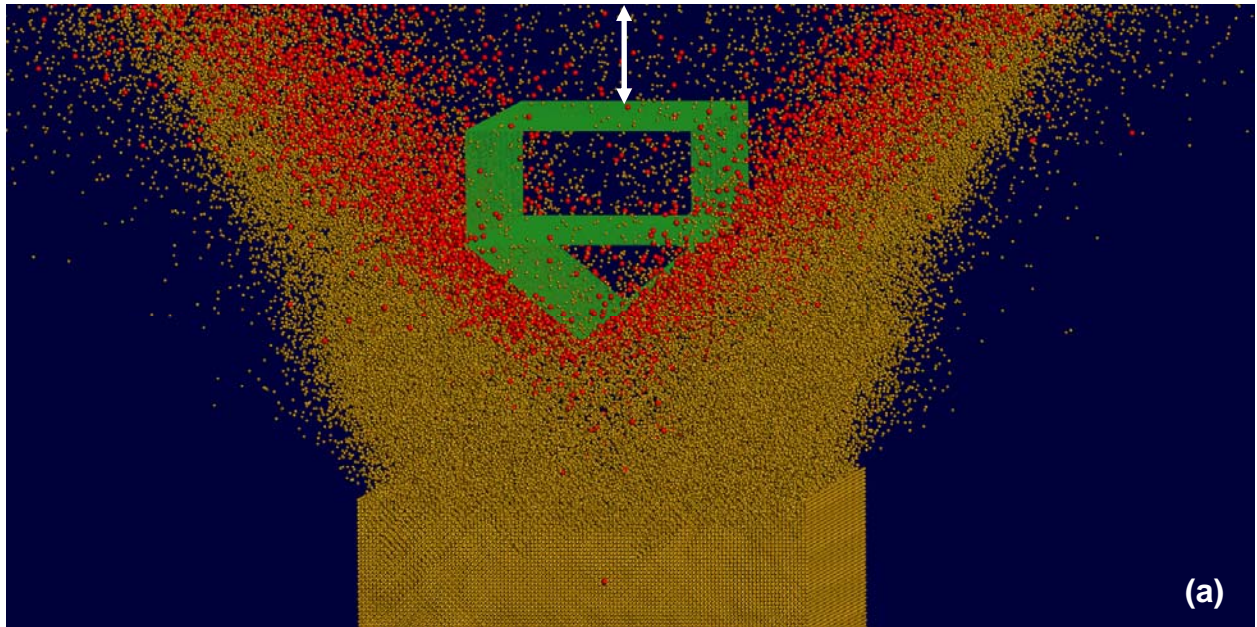


**Figure 9. Spatial distribution of soil, HE detonation products and steel used to make rigid SBS at a fixed (12 ms) post-detonation time for the case of (a) the SBS configuration without channels; (b) the SBS configuration with constant cross-section channels; and (c) the baseline SBS configuration with flared channels.**

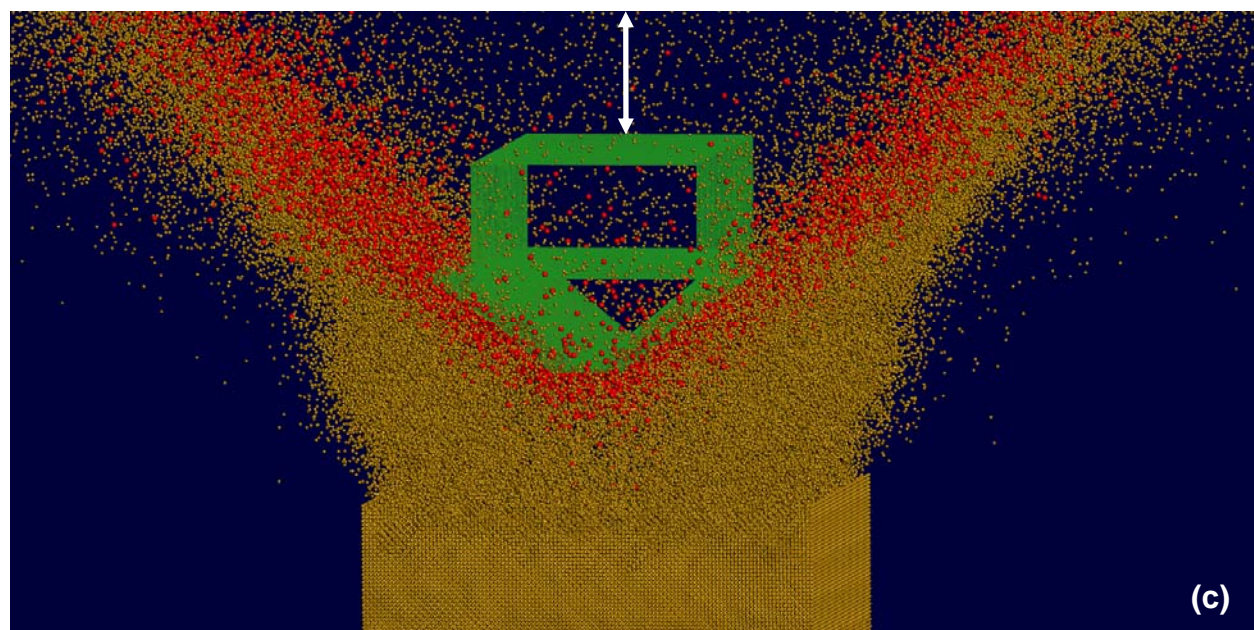


**Figure 9. Continued.**



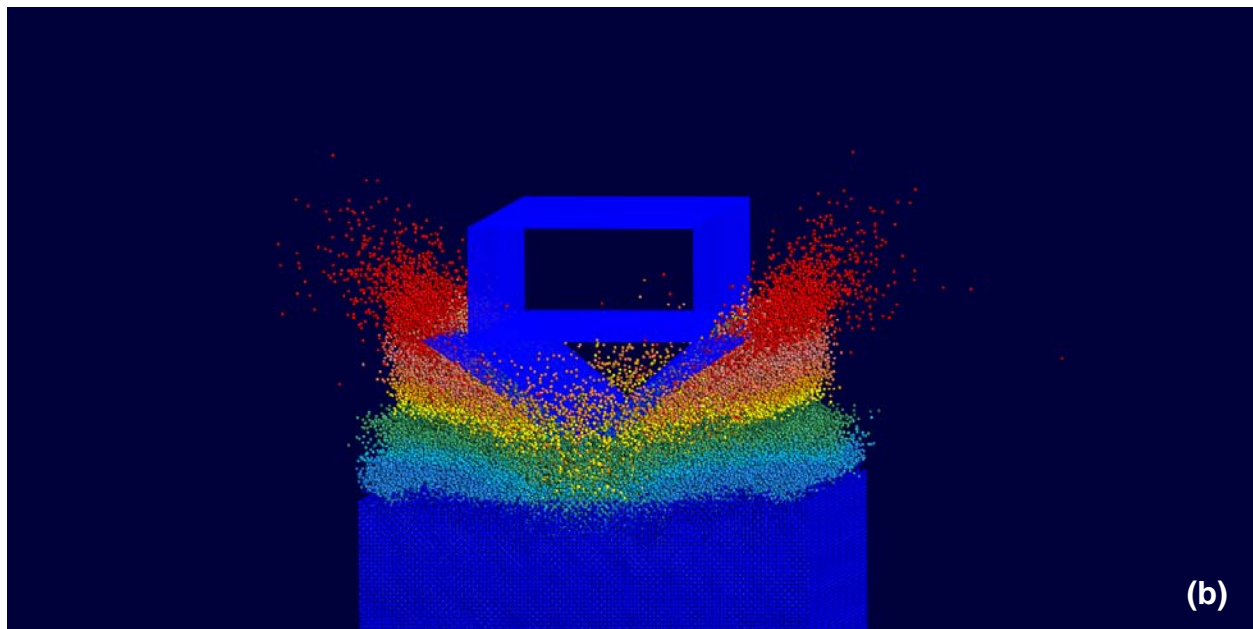
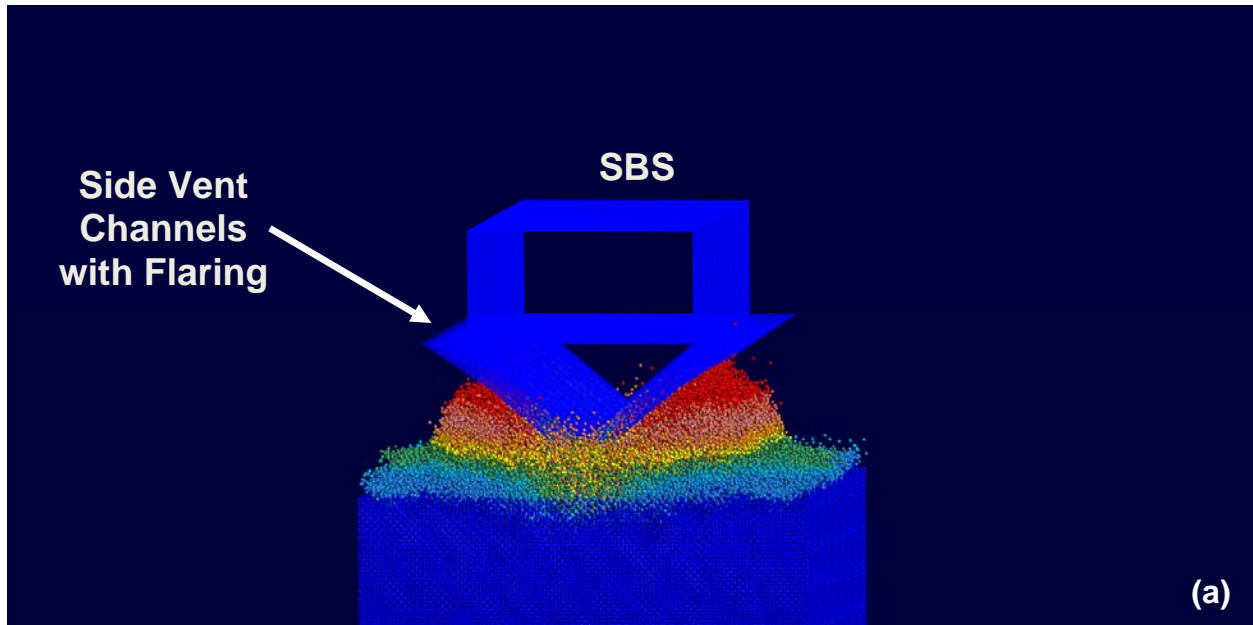


**Figure 10. Spatial distribution of the velocities of the soil and mine-detonation-product particles and rigidized-SBS in the case of the baseline SBS configuration at post-detonation times of: (a) 2 ms; (b) 4 ms; (c) 6 ms; and (d) 8 ms.**

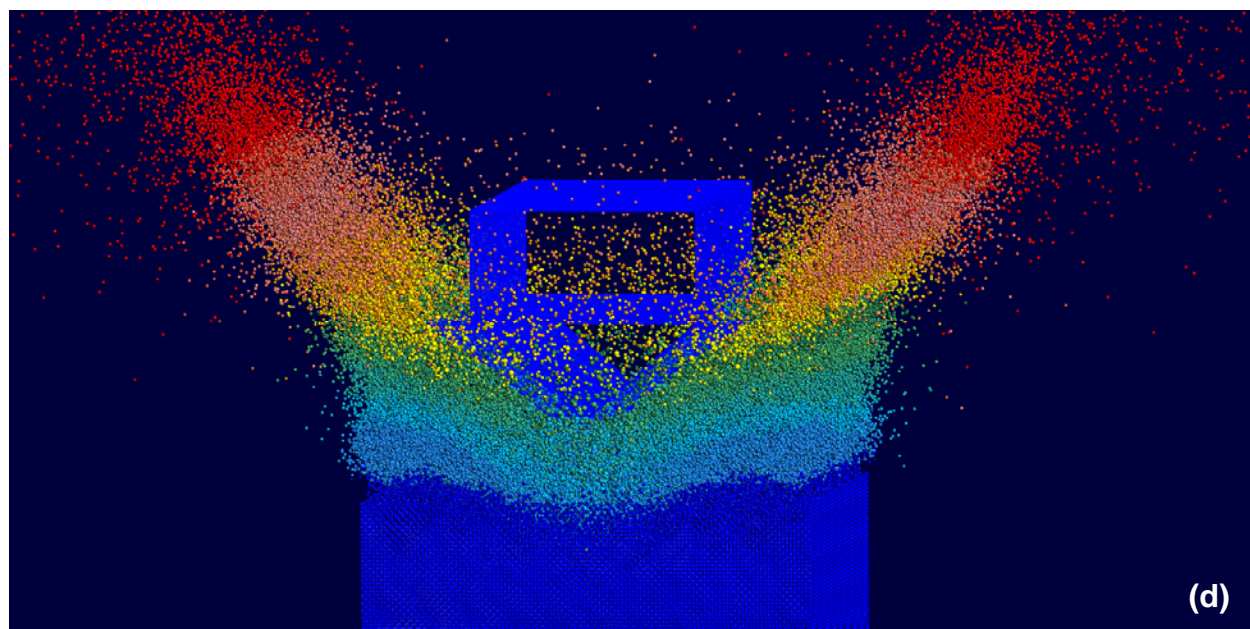
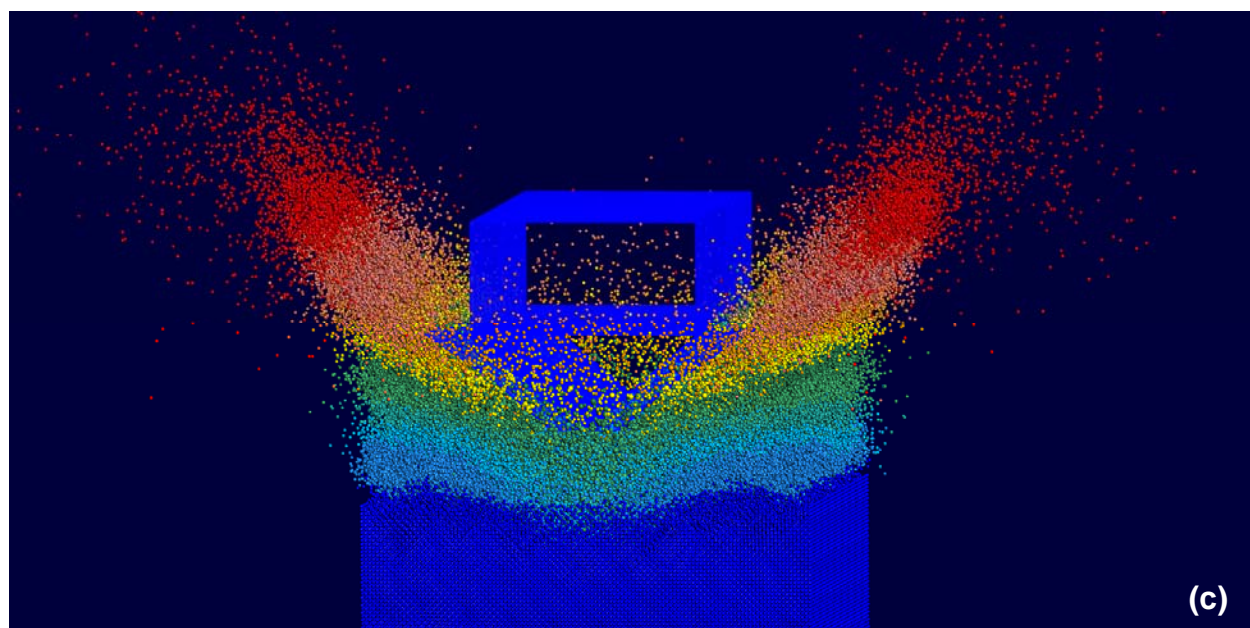


**Figure 10. Continued.**



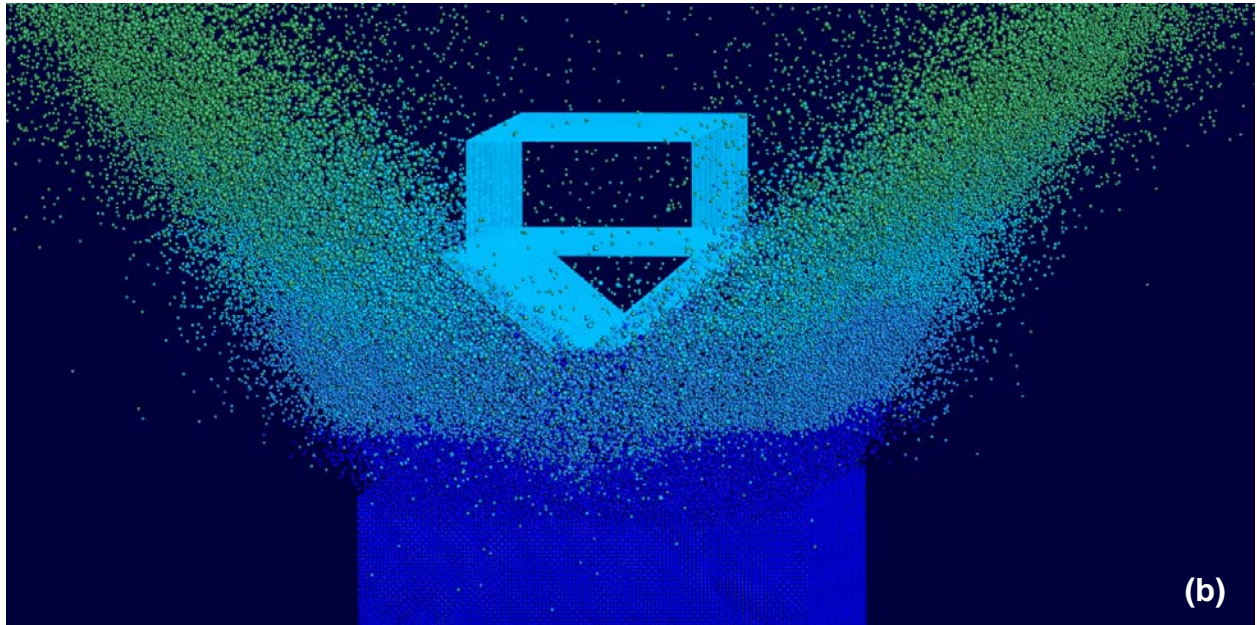
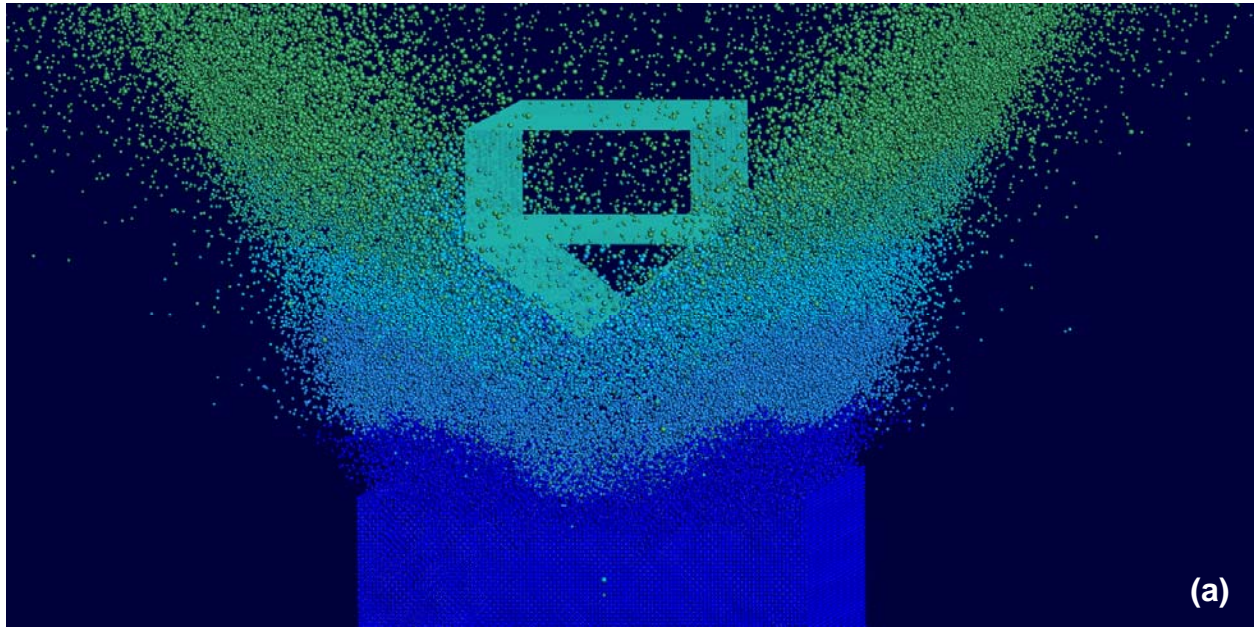


**Figure 11. Spatial distribution of the velocities of the soil and mine-detonation-product particles and rigidized-SBS at a fixed (12 ms) post-detonation time for the case of (a) the SBS configuration without channels; (b) the SBS configuration with constant cross-section channels; and (c) the baseline SBS configuration with flared channels.**

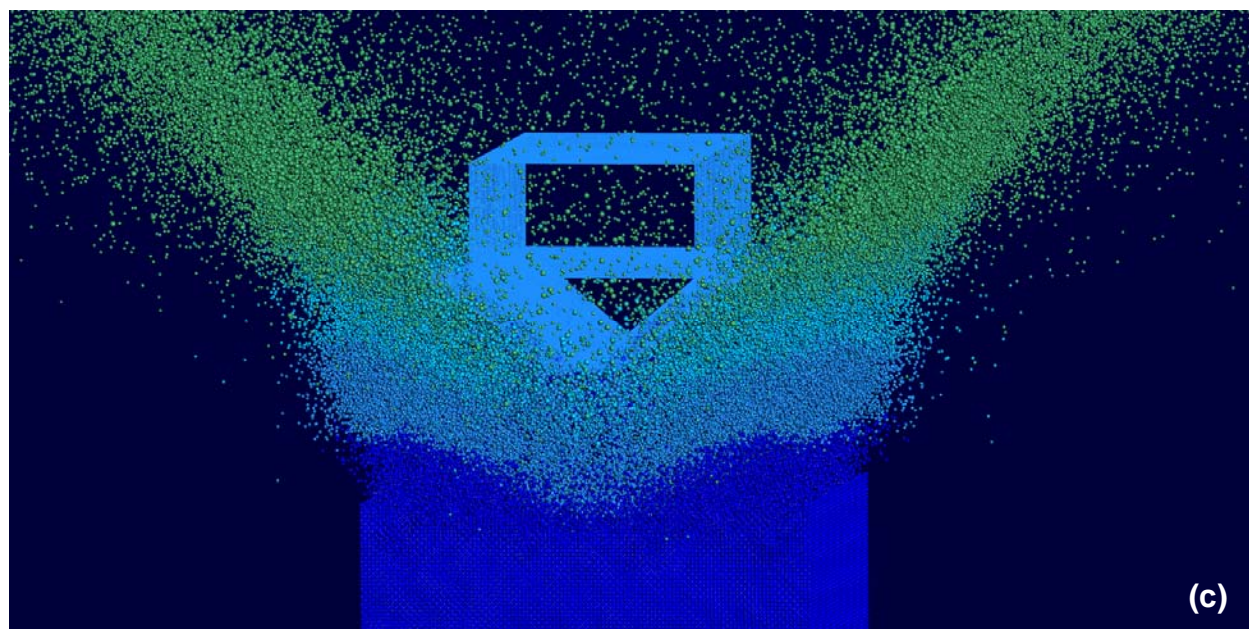


**Figure 11. Continued.**



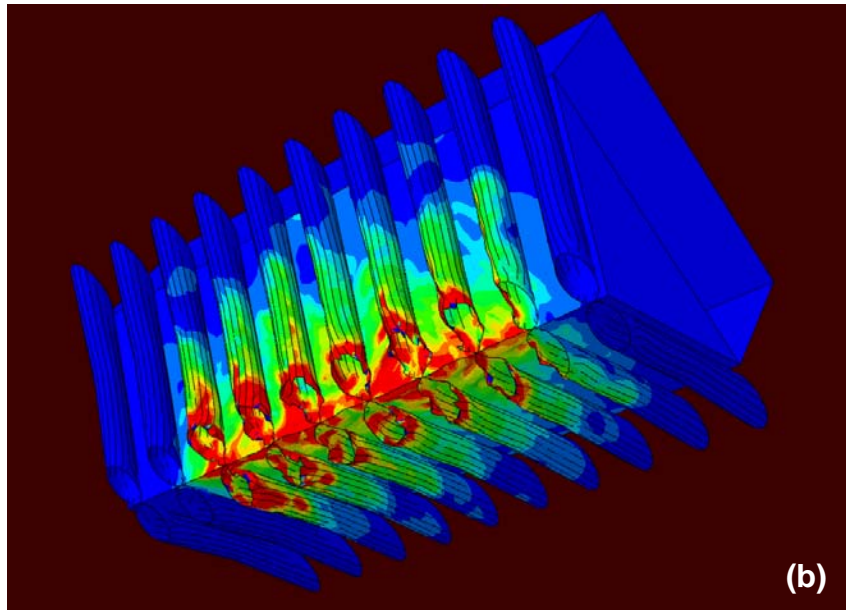
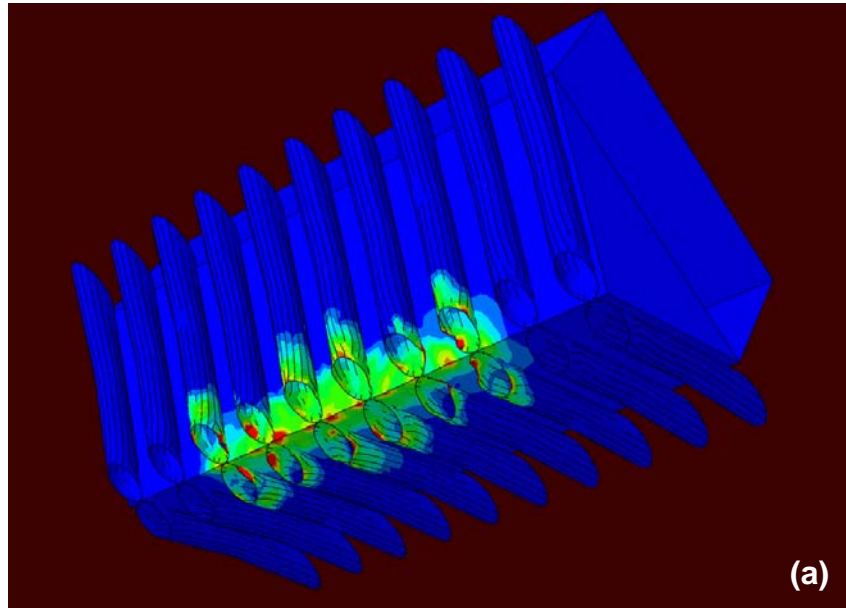


**Figure 12. Temporal evolutions of the SBS steel material and the associated von Mises stress at post-detonation times of: (a) 2 ms; (b) 4 ms; (c) 6 ms; and (d) 8 ms.**

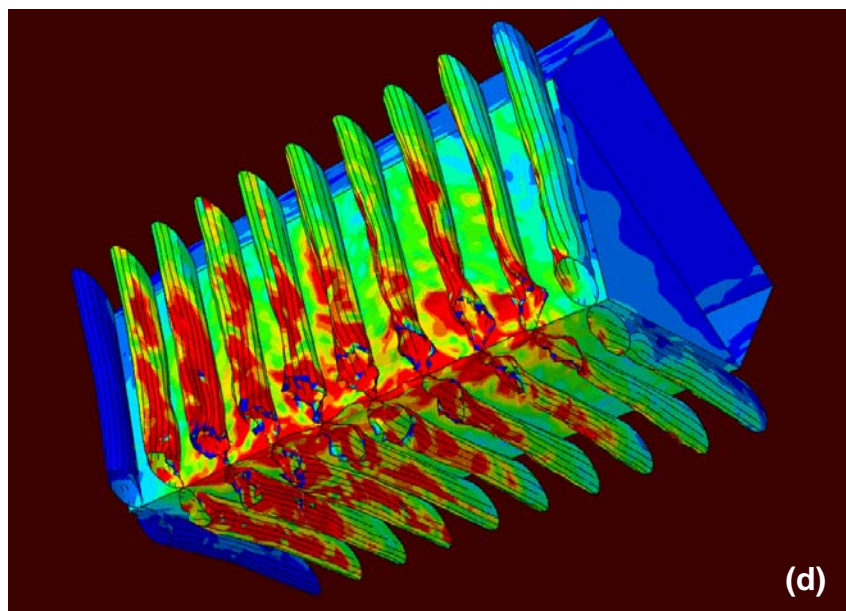
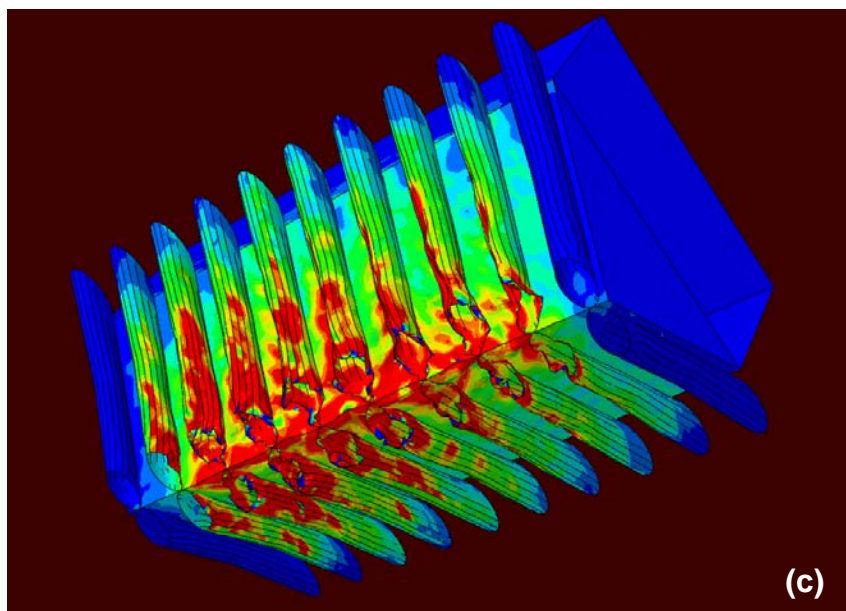
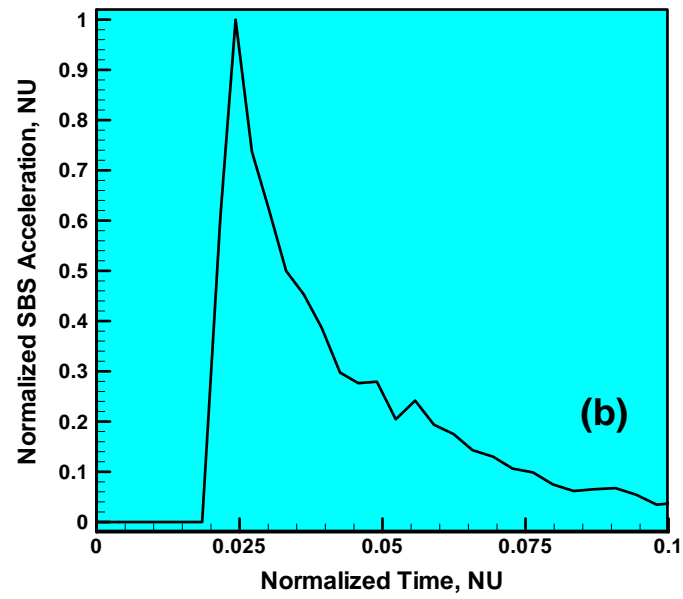
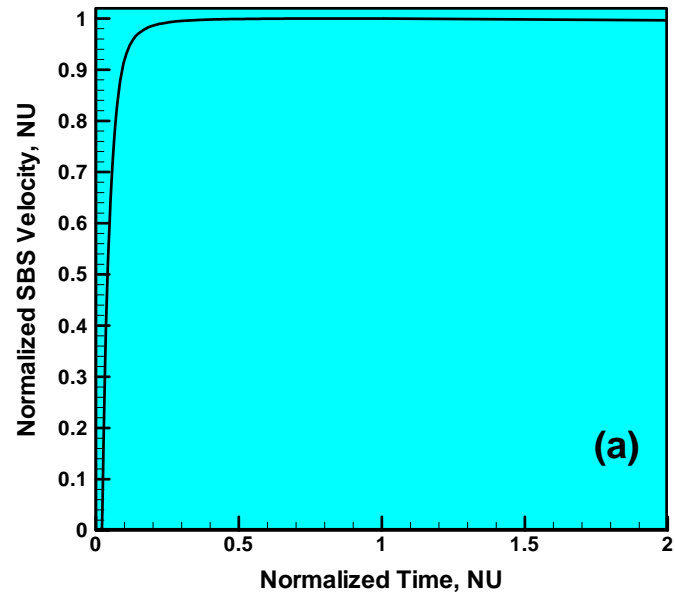
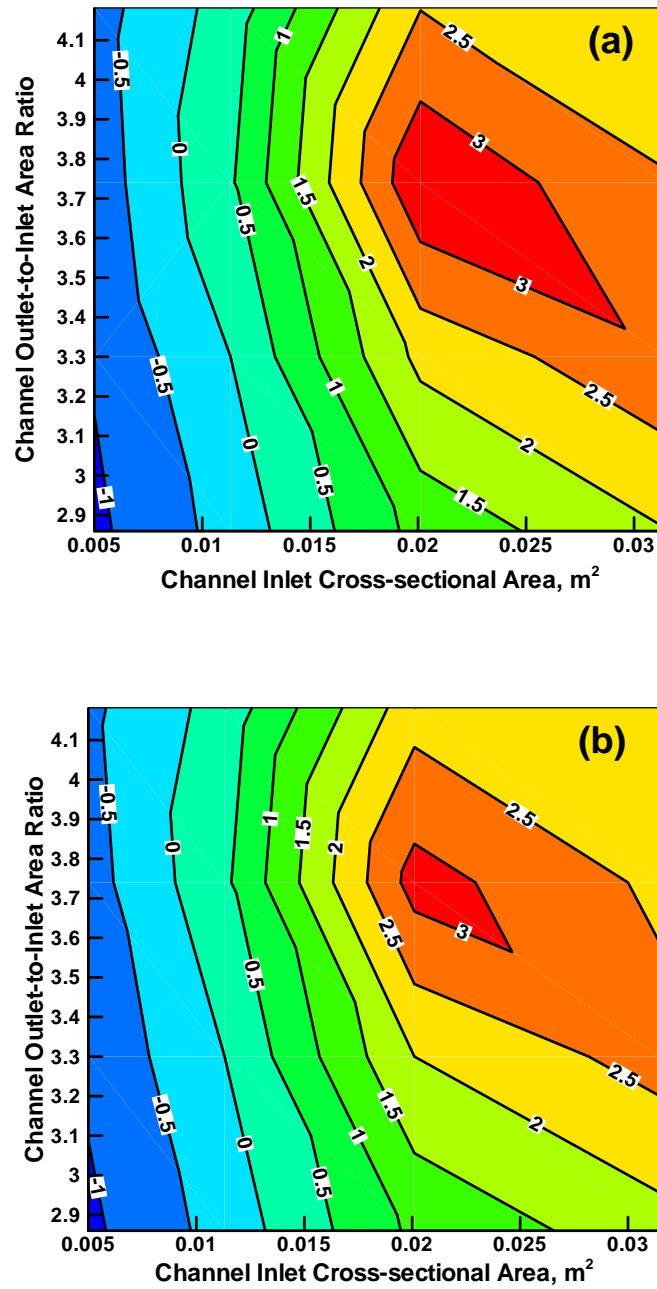


Figure 12. Continued.



**Figure 13. Examples of the typical: (a) SBS normalized-velocity vs. time; and (b) SBS normalized-acceleration vs. time results obtained in the present work.**



**Figure 14. Percent reduction (relative to the SBS case without side-vent channels) in total blast momentum for the baseline SBS configuration as a function of channel inlet-area and inlet-to-outlet area ratio: (a) present combined finite-element/discrete-particle analysis; and (b) combined Eulerian/Lagrangian analysis presented in Ref. [1].**

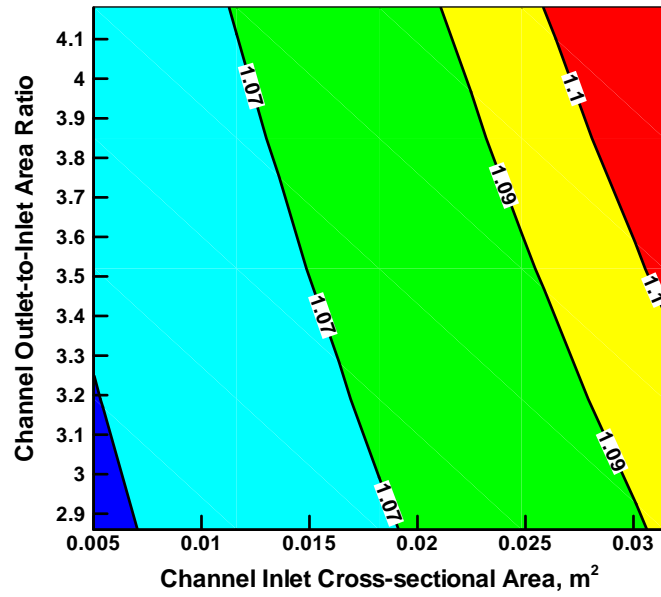


**Figure 15.** Percent increase (relative to the SBS case without side-vent channels) in the mass of the baseline SBS configuration as a function of channel inlet-area and inlet-to-outlet area ratio.

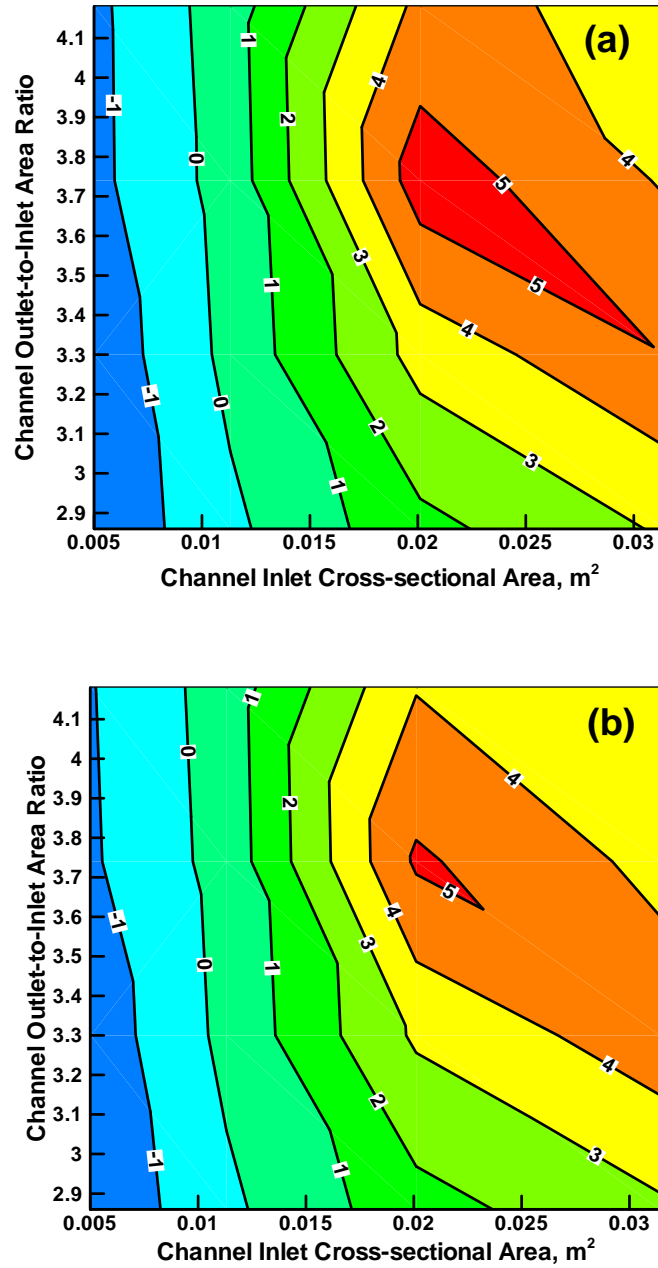


**Figure 16.** Percent reduction (relative to the SBS case without side-vent channels) in total kinetic energy for the baseline SBS configuration as a function of channel inlet-area and inlet-to-outlet area ratio: (a) present combined finite-element/discrete-particle analysis; and (b) combined Eulerian/Lagrangian analysis presented in Ref. [1].

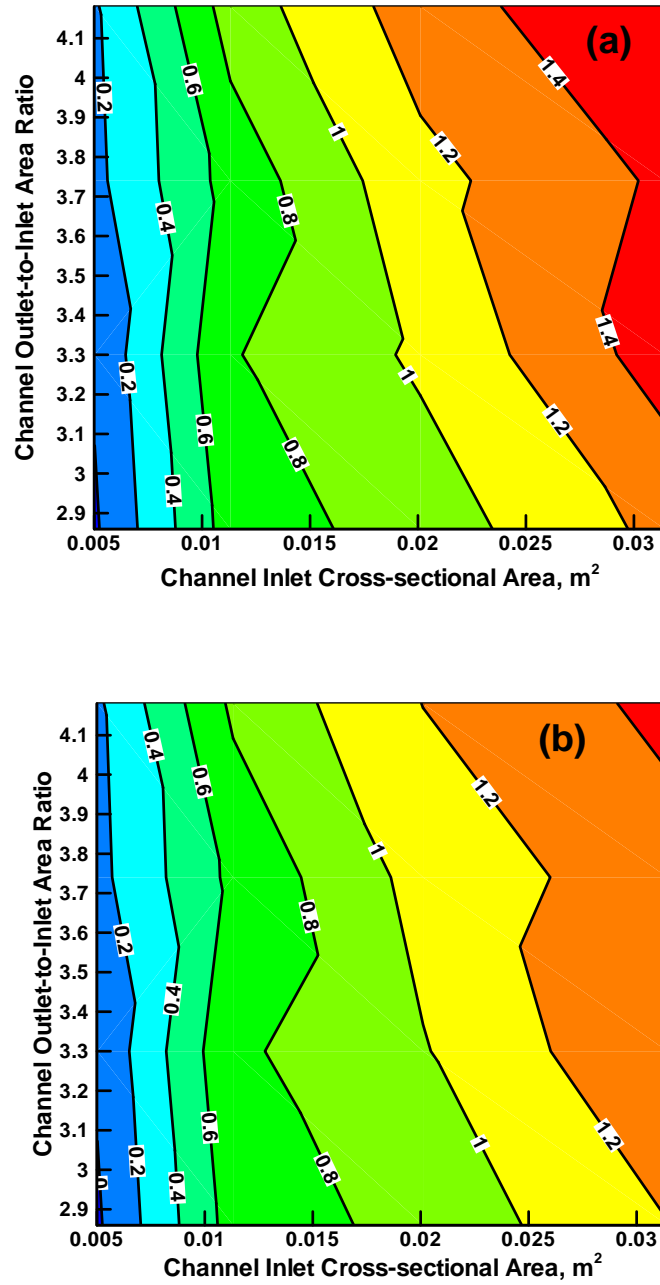


**Figure 17. Percent reduction (relative to the SBS case without side-vent channels) in maximum acceleration for the baseline SBS configuration as a function of channel inlet-area and inlet-to-outlet area ratio: (a) present combined finite-element/discrete-particle analysis; and (b) combined Eulerian/Lagrangian analysis presented in Ref. [1].**